Pontificia Universidad Católica de Chile
Facultad de Física
Instituto de Astrofísica

A VLT/MUSE galaxy survey towards QSO Q1410: looking for a WHIM traced by BLAs in inter-cluster filaments

BY

Ismael Alejandro Pessa Gutiérrez

Tesis presentada a la Facultad de Física de la Pontificia Universidad Católica de Chile, para optar al grado académico de Magíster en Astrofísica.

Supervisor : Dr. Nicolás Tejos
Dr. Luis Felipe Barrientos
Correctors :

May 7th, 2018
Santiago, Chile

Declaration

The work described in this thesis was undertaken between 2016 and 2018 while the author was a researcher student under the supervision of Professor L. Felipe Barrientos and Dr. Nicolas Tejos, in the institute of astrophysics at the Pontificia Universidad Católica de Chile. This work has not been submitted for any other degree at the Pontificia Universidad Católica de Chile or any other university.

This work has been published in the following paper:

- *A VLT/MUSE galaxy survey towards QSO Q1410: looking for a WHIM traced by BLAs in inter-cluster filaments*, Ismael Pessa, Nicolas Tejos, L Felipe Barrientos, Jessica Werk, Richard Bielby, Nelson Padilla, Simon L Morris, J Xavier Prochaska, Sebastian Lopez, Cameron Hummels; Monthly Notices of the Royal Astronomical Society, Volume 477, Issue 3, 1 July 2018, Pages 2991-3013

Most of the work in this thesis was completed by the author. Those part not done by him are included in the following list:

- In Appendix E, the revision to the BLAs was performed by Nicolas Tejos. The author used this revision to look for potential systematic uncertainties in the characterization of the BLAs.

To Paz Bluhm

Acknowledgements

I am deeply grateful to my parents, Carmen and Natalio, for their unconditional love and support through my career and life in general. And I am also thankful to my sisters, Natalia and Alejandra, for being an inspiration to follow my dreams and live the life that I want. My sincere gratitude to Paz Bluhm, thank you for so many things, for your trust and love, and for making me happy every day. Thanks to Nicolas Tejos for being an excellent supervisor. I am grateful for teaching me so much during this years, to be perfectionist and critical, in particular with my own work, I have grown a lot as a scientist and as a person with his support. I also thank Felipe Barrientos for his suggestions and ideas through this investigation. I have had a great time in Pontificia Universidad Católica de Chile and I had the opportunity to meet very nice people. Special thanks to my office mates Rafael and Jonathan, always keeping a great working atmosphere.

Contents

List of Figures

Resumen

Simulaciones cosmológicas predicen que una fracción significativa de los bariones a bajo redshift residen en los filamentos de la llamada red cósmica en forma de plasma difuso a temperaturas $T \sim 10^5 - 10^7$ K. Sin embargo, la cofirmación observacional definitiva de este gas (warm-hot intergalactic medium, o WHIM) ha sido esquiva. En el paradigma de ΛCDM, los cúmulos de galaxias corresponden a nodos en la red cósmica, donde se intersectan varios filamentos. En un trabajo previo, usamos datos de HST/COS para construir el primer survey de absorciones anchas de hidrógeno neutro (broad Lyα absorbers, o BLAs) potencialmente producidas por el WHIM en filamentos conectando cúmulos. En el espectro de un QSO en particular (Q1410), cuya linea de visión intersecta 7 ejes inter-cúmulos independientes con parámetros de impacto < 3 Mpc (comoving), se encontró un exceso de BLAs en un factor 4 respecto al valor promedio esperado. En este trabajo, investigamos el origen de estos BLAs, caracterizando todas las galaxies dentro del campo de Q1410 usando VLT/MUSE. Identificamos 77 fuentes y obtuvimos el redshift para 52 de ellas. De un total de 7 BLAs en ejes inter-cúmulos, encontramos que 3 *no presentan* ninguna galaxia cercana dentro de nuestros límites de luminosidad ($\sim 4 \times 10^8$ L$_\odot$ $\sim$0.01 L$_*$), esto evidencia que estos BLAs podrían representar detecciones de WHIM genuinas. Combinandos esta muestra con otros BLAs en la literatura podemos inferir un valor de $\Omega_{\rm bar}^{\rm fil} = 0.02-0.04$ para el contenido de bariones en los filamentos. Nuestras estimaciones son consistentes con las predicciones de simulaciones numéricas, pero están sujetas a importantes incertezas sistemáticas, principamente de la geometría asumida para el sistema, la fracción de ionización y el perfil de densidad del gas dentro de un filamento.

Abstract

Cosmological simulations predict that a significant fraction of the low-z baryon budget resides in large-scale filaments in the form of a diffuse plasma at temperatures $T \sim 10^5 - 10^7$ K. However, direct observation of this so-called warm-hot intergalactic medium (WHIM) has been elusive. In the ΛCDM paradigm, galaxy clusters correspond to the nodes of the cosmic web at the intersection of several large-scale filamentary threads. In previous work, we used HST/COS data to conduct the first survey of broad HI Lyα absorbers (BLAs) potentially produced by WHIM in inter-cluster filaments. We targeted a single QSO, namely Q1410, whose sight-line intersects 7 independent inter-cluster axes at impact parameters < 3 Mpc (co-moving), and found a tentative excess of a factor of ∼4 with respect to the field. Here, we further investigate the origin of these BLAs by performing a blind galaxy survey within the Q1410 field using VLT/MUSE. We identified 77 sources and obtained the redshifts for 52 of them. Out of the total sample of 7 BLAs in inter-cluster axes, we found 3 *without* any galaxy counterpart to stringent luminosity limits ($\sim 4 \times 10^8$ L$_\odot$ ∼0.01 L$_*$), providing further evidence that these BLAs may represent genuine WHIM detections. We combined this sample with other suitable BLAs from the literature and inferred the corresponding baryon mean density for these filaments in the range $\Omega_{\rm bar}^{\rm fil} = 0.02 - 0.04$. Our rough estimates are consistent with the predictions from numerical simulations but still subject to large systematic uncertainties, mostly from the adopted geometry, ionization corrections and density profile.

Chapter 1

Introduction

The current cosmological paradigm predicts that only ∼4.8% of the energy content in the Universe is in the form of baryonic matter (Planck Collaboration et al. 2016). At higher redshifts ($z \gtrsim 3$) about 90% of the baryons are assembled in the diffuse photoionized intergalactic medium (Weinberg et al. 1997) that give raise to the so called Lyα Forest. Redshifts of $z = 2-5$ set the bases of our understanding of intergalactic matter. This redshift range has been so important firstly because at z $\gtrsim$ 2 the Lyα line (as well as some of the most useful metal lines, particularly C IV $\lambda\lambda$1548, 1551Å and O VI $\lambda\lambda$1032, 1038Å) has redshifted sufficiently that it can be observed with ground-based optical telescopes and, secondly, because there are plenty of bright quasars that enable high signal-to-noise (S/N) spectra at high-resolution. In addition, at these times the density and ionization state of the IGM are ideal for probing gas near the cosmic mean density with the HI Lyα forest. The Lyα forest spectral region of hundreds of quasars has been observed at high resolution with 10 m telescopes see (see O'Meara et al. 2015), and the number has surpassed a hundred thousand at medium resolution on the 2.5 m Sloan telescope (Lee et al. 2013). These quasar spectra have been used to conduct precision tests of the Lyα forest, to measure the H I column density distribution and and to measure the enrichment of intergalactic gas (McQuinn 2016, and references therein)

In contrast, in the local Universe the fraction of baryons in the diffuse photoionized

IGM is only ∼30% (Penton et al. 2004; Lehner et al. 2007). From the remaining baryons, only ∼30%−40% are found in other well studied phases (e.g. Stars, ISM, Cluster gas) (Davé et al. 2001), leaving ∼40%−30% of the low-z baryons unaccounted for. This is the so-called 'missing baryons problem' on cosmic scales, where a significant fraction of the total baryons are missing in the z<1 Universe (Persic & Salucci 1992; Fukugita et al. 1998; Prochaska & Tumlinson 2009; Shull et al. 2012).

Different hydrodynamical cosmological simulations based on ΛCDM cosmology have predicted that ∼30%−40% of the total baryons at low redshift would be in the warm-hot intergalactic medium (WHIM), at temperatures between $10^5 - 10^7$ K particularly residing in diffuse filamentary large-scale structures with a median overdensity of ∼10−30 times the mean density of the Universe (Cen & Ostriker 1999; Davé et al. 2001). This is because at the present epoch, hierarchical structure formation model has had time to produce deeper potential wells where baryonic matter is accreted and heated due to the gravitational shocks produced by its collapse. As a consequence of this shock heating, almost all the hydrogen is ionized (by collisional processes or UV radiation) and only a small fraction remains neutral ($f_{\rm HI}$∼10^{-5} in a pure collisional ionization scenario; Sutherland & Dopita 1993; Richter et al. 2004)).

The definitive observational confirmation of the WHIM has been elusive because of the low expected column density of HI in the hot gas ($N_{\rm HI} \approx 10^{13}\,{\rm cm}^{-2}$) (Richter et al. 2006) and large Doppler parameters (tipically $b \geq 40\,{\rm km\ s}^{-1}$; from thermal and non-thermal processes) that would place the absorption features produced by the WHIM at the limit of detectability (e.g. Cen & Ostriker 1999; Davé et al. 2001). Emission of this plasma is also expected in the UV and X-ray, and marginal detections have been reported (e.g. Hattori et al. 2017); a firm detection in emission still awaits more sensitive telescopes (Fang et al. 2005). More recently, Tanimura et al. (2017) and de Graff et al. (2017) have reported statistically significant detections ($> 5\sigma$) of warm-hot baryons through the thermal Sunyaev-Zel'dovich effect signal in a sample of stacked filaments connecting massive haloes. They established a gas density of ∼6 times the mean universal baryon density,

accounting for ~30% of the total baryon budget. However, absorption line techniques may still represent our current best chance to detect *individual* WHIM signatures, particularly through broad HI Lyα absorptions (BLA) in the FUV spectra of bright QSOs.

Previous studies have detected BLAs potentially produced by WHIM at low redshifts (Richter et al. 2006; Tripp et al. 2006; Lehner et al. 2007; Danforth et al. 2010; Tilton et al. 2012; Wakker et al. 2015). Richter et al. (2006) calculated the incidence of BLAs per unit redshift to be $dN/dz \approx 22$ using 4 different QSO sight-lines and derived a lower limit for the baryon content of BLAs $\Omega_{\rm BLA} > 0.0027 h_{70}^{-1}$. These results are subject to the uncertainty that not every BLA detected in the FUV QSO spectrum is necessarily related to the WHIM and the authors estimated an associated systematic error as high as 50%, that could lead to an overestimation of $\Omega_{\rm BLA}$. These studies assume collisional ionization equilibrium, but according to simulations (Fang & Bryan 2001), photoionization by the UV background also becomes important at typical WHIM densities. Neglecting photoionization can conversely lead to underestimation of the baryon density. Bonamente et al. (2016) used *Chandra* spectra and found an absorption line identified as O VIII that could potentially be the *X*-ray counterpart of the FUV BLA detected by Tilton et al. (2012). Indeed, from the SDSS data Bonamente et al. (2016) found evidence of a large-scale filament structure at nearly the same redshift as the absorption features. Wakker et al. (2015) used HST spectra of 24 AGN to sample the gas in a low-z filament, by measuring the properties of 15 Lyα absorbers in the AGN spectra that are likely associated to the intergalactic gas of the filament. In particular, they studied the properties of the gas as a function of the impact parameter to the filament axis and found evidence that the Lyα line-width anticorrelates with the filament impact parameter. Furthermore, the authors found 4 BLAs in this sample, all of them in the sight-lines passing relatively close (< 540 kpc) to the axis of the filament, which would suggest an increase in temperature and/or turbulence.

In this thesis, we aim at establishing a more accurate relation between BLAs and the WHIM. Tejos et al. (2016) performed a novel experiment, searching for BLA features

potentially produced by the WHIM at the redshifts where large-scale filaments should exist. They targeted a single QSO at $z \sim 0.79$ (SDSS J141038.39+230447.1; hereafter referred to as Q1410) whose unique sight-line passes throughout 7 independent cluster pairs at $0.1 < z < 0.5$, with impact parameters < 3 Mpc to the inter-cluster axes connecting them. Theoretical models predict a high probability of finding a filamentary structure between close ($\lesssim 20$ Mpc) and massive ($\gtrsim 10^{14} M_{\odot}$) galaxy cluster pairs (e.g. Colberg et al. 2005; González & Padilla 2010; Aragón-Calvo et al. 2010). The authors identified 7 BLAs with Doppler parameters > 50 km s^{-1} in the spectrum of Q1410 at similar redshifts for 6 out of the 7 cluster pairs and found a tentative excess of BLAs of a factor of ∼4 with respect to the field. These BLAs now became potential WHIM signatures and are the subject of further investigation presented in this thesis.

We aim at determining the origin of these BLAs, in particular to assess whether these absorption features are produced by the intergalactic medium (IGM) or by the halos of intervening galaxies (e.g. Williams et al. 2013). To discern between these cases, we used the physical impact parameter of nearby galaxies to the Q1410 sight-line and the relative velocity offset between these galaxies and the BLAs. To this end, we have conducted a blind galaxy survey using the VLT/MUSE IFU (Bacon et al. 2014), with particular emphasis on the presence or lack of galaxies at the redshifts of the reported BLAs. Our survey used 1 hour of VLT/MUSE integration time, reaching redshift completeness level of $\sim 75\%$ down to magnitude $r_{\rm AB} = 25$ mag.

This thesis is structured as follows. In Chapter 1 we present and describe our data and methods used. In Chapter 2 we describe our survey, including the identification, characterization, completeness and limitations. Chapter 3 presents our main results and in Chapter 4 we discuss them. A summary of our results and conclusions are presented in Chapter 5. For our analysis, we assume a ΛCDM cosmology based on the results of the Planck Collaboration et al. (2016).

Chapter 2

Data and Methods

2.1 Line absorption technique

Due to the extremely low densities of the ionized IGM, the currently most feasible way to observe it is through intervening absorption line systems in the spectra of bright background sources. The idea behind this is to use a source with a known spectrum, and look for absorptions that are inconsistent with being part of the source itself (e.g. Gunn and Peterson, 1965; Greenstein and Schmidt, 1967; Burbidge et al., 1968). The interpretation of these absorption features is that they were produced by intervening gas in the line of sight, and its redshift can be determined from the observed wavelength of the identified transition (e.g. see Rauch, 1998, for a review). QSOs are the most popular background source used to this end, but because of QSOs are punctual sources, this technique is limited to be a one-dimensional characterization of the IGM (although recent works have used a bright lensed galaxy as the background source to perform a two-dimensional characterization of the intervening gas). On the other hand, this technique allows the tracing of extremely weak column densities of gas in a fairly unbiased way. The main relevant observables of these absorption lines are redshift, column density and Doppler parameter. The column density is given by the quantity of absorbing material along the line of sight and the Doppler parameter is given by the width of the line. The classical approach to obtain their

value is fitting a Voigt profile to the absorption feature. This Voigt profile results from the convolution of a Gaussian profile to parametrize the thermal broadening of the gas and a Lorentzian profile to approximate the natural profile of the line. Because of the uncertainty principle, the transition wavelength is not perfectly constrained, and there is a probability of absorption at different wavelengths. This probability function can be approximated by the Lorentzian profile. Tejos et al. (2016) used this technique to identify and characterize the BLAs on the spectrum of a QSO that will be the main subject of the further study. Since a BLA is tracing warm-hot gas, in a purely thermal broadening scenario we expect values higher that 40 km s^{-1} for the Doppler parameter b (This is the corresponding value for gas at $T \approx 10^5$ K. However, since there may be an additional non-thermal broadening contribution, such as turbulence of the gas, we may expect even higher values for the Doppler parameter for the BLAs that are actually tracing WHIM.

2.2 Integral Field spectroscopy

Integral field spectroscopy (IFS) is a mode of instrumentation that enables spectra to be obtained of a two-dimensional region of the sky, combining spectroscopic and imaging capabilities. The final product of these observations is (usually) a data-cube, with 2 spatial coordinates and the third wavelength axis. Integral field spectroscopy has demonstrated to be a powerful tool to study the physical properties of extended astronomical objects (e.g. kinematics and chemical distribution) or to search for extremely faint objects (e.g. with low continuum level but with emission lines), among others. MUSE (Bacon et al. 2014) is the first large integral field spectrograph ever installed at an 8-meter telescope. It uses 24 spectrographs to separate light into its component colors to create both images and spectra of its field of view.

VLT/MUSE observations			
Pointings		Exposure time	PA
RA	DEC	s	deg
14:10:38.39	+23:04:47.18	2×900	0
14:10:39.79	+23:05:00.80	2×900	90

Table 2.1: Summary of our observations described in Chapter 3.

2.3 Data

2.3.1 VLT/MUSE Integral field spectroscopy

We obtained VLT/MUSE data of a $\sim 1 \times 1$ arcmin^2 field containing Q1410 as part of the ESO programme 094.A-0575 (PI Tejos). The observations were taken with a seeing of ~0.8", sampled at 0.2×0.2 arcsec^2, with a spectral range from 4750 – 9350 Å, and a resolving power $R \sim 1770 - 3590$. A total of 4 exposures of 15 min each were used, 2 of them centered on the Q1410 field with a position angle PA= 0° and the remaining 2 centered on the brightest nearby galaxy at RA=14h10m39.8s and Dec.=+23d05m00.8s (J2000; ΔRA≈19.4", ΔDec.≈14.2") with a PA=90°. As a result of this double pointing we obtained higher signal-to-noise data where the 2 fields overlap for a full 1 hr exposure. In the edges, the effective exposure time is 30 min. Table 2.1 summarizes these observations and Fig. 3.2 shows the targeted MUSE field (grey contours). Datacubes have been reduced and combined using the standard MUSE pipeline version muse-1.4 (see `http://www.eso.org/observing/dfo/quality/PHOENIX/MUSE/processing.html` for details). As a post-processing reduction, we used the ZAP software (Soto et al. 2016) to perform a second order sky subtraction, which uses principal components analysis (PCA) to isolate and remove residual sky subtraction features.

2.3.2 VLT/VIMOS Imaging

Additional VLT/VIMOS data are available for this field. In particular, 2 min *R*-band pre-imaging was obtained as part of ESO programme 094.A-0575 (PI Tejos) for the mask preparation of multi-object spectroscopy (MOS) on the field. Unfortunately, the MOS data were never obtained. However, we are able to use the pre-imaging data as an astrometry reference frame for our MUSE data (see Fig. 3.2).

Chapter 3

Galaxy Survey

3.1 Source Identification

To identify the sources in the field and determine the aperture that best defines the spaxels[1] within each source we used SExtractor (Bertin & Arnouts 1996) in the 'white image'. This image corresponds to the sum of the flux at all wavelengths for each spaxel. After performing a visual inspection to remove artifacts, we manually added 10 sources that were not detected by SExtractor but were still visible (but faint) in the 'white image'. Finally, we used MUSELET (for MUSE Line Emission Tracker) a SExtractor-based python tool to detect emission lines in a datacube included in the MPDAF Python package (Bacon et al. 2016) to search for additional emission-lines-only galaxies that were not visible in the 'white image' but show at least one strong emission line, and we added 1 source.
After this, we searched for additional undetected emission-line galaxies at the redshifts of the cluster-pairs by collapsing the wavelengths of the cube that would contain strong emission lines at a given redshift, but we did not find any previously-undetected galaxy. We ended up with a sample of 77 sources in the MUSE FoV, including the central QSO. For each source we extracted a 1-D spectrum combining the spaxels inside the source aperture. The flux on each spaxel was weighted by a 'bright profile', proportional to the total flux

[1]We refer to spaxel as a spatial sampling element, that correspond to a one-pixel spectrum in the datacube.

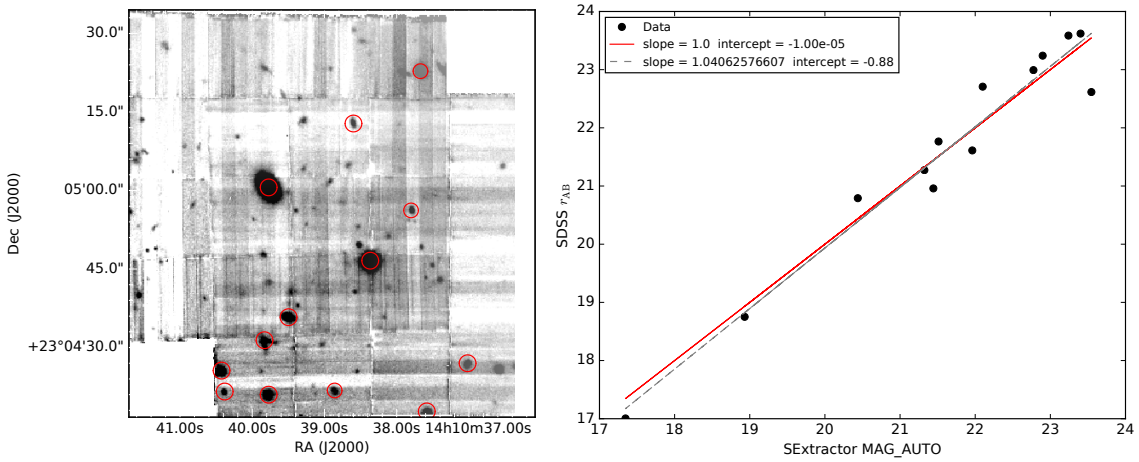

Figure 3.1: *Left*: Red circles mark the sources in the MUSE field of view that were used for the photometric cross-match with the SDSS magnitudes. *Right*: Black dots represent the SDSS r_{AB} magnitude of the sources marked in the left panel as a function of their SExtractor MAG_AUTO determined in our survey, corrected by a zero-point of 35.119. The zero-point was determined as the intercept of the same fit, using the uncorrected MAG_AUTO value. The continuum red line is the best linear fit with a slope of unity between both magnitudes. The dashed gray line is the best linear fit, for comparison. The zero-point obtained was used to calibrate the photometry of the full sample.

of that spaxel in the white image. For the sources that were not originally detected by SExtractor, the aperture was arbitrarily defined as a circle containing most of the apparent flux. We estimated the r_{AB} magnitude for all the sources by convolving the datacube fluxes with a SDSS r transmission curve. This effectively creates a MUSE r-image. The zero-point of this image was calibrated by doing a linear fit with slope of unity between the SDSS modeled magnitudes and the SExtractor MAG AUTO magnitudes[2] of several cross-matched sources in the field as is shown in Fig. 3.1 (the photometry was only computed for the sources detected by SExtractor). Our identified sources are summarized in Tables 3.1 and 3.2

[2]We expect that the flux lost by the aperture defined by SExtractor accounts for less than 0.1 mag.

3.2 Source characterization

Redshifts of each source were measured using Redmonster (Hutchinson et al. 2016). The code performs a χ^2 minimization between the observed spectrum and a set of theoretical models for galaxies, stars and QSOs. These templates are modulated by a low-order polynomial mimicking the effects of galactic extinction, sky-subtraction residual and possible spectrophotometric errors. We adopted a reliability scheme for the redshifts measurements as follows:

- 'a' sources: these are the best characterized, showing at least 2 well characterized features in their spectra.
- 'b' sources: these are relatively well characterized, showing at least 1 well identified feature and a possible second feature (marginal) in their spectra.
- 'c' sources: these are uncertain, showing only one feature in their spectra (typically a single emission line). We included 'c' sources in our analysis in order to be conservative for ruling out the presence of galaxies near BLA features.
- 'd' sources: these could not be characterized as they did not show any spectral feature. Most of them are fainter than $r_{\rm AB} = 24$ mag, and were excluded from our analysis.

Out of the 77 sources, we successfully obtained the redshifts for 52 of them (see Tables 3.1 and 3.2). These include 42 obtained with Redmonster and 10 from visual inspection of strong emission lines. In Appendix D we present the Redmonster fits for the galaxies with a reliability level of 'a', 'b' and 'c'. For the galaxies showing only one strong emission line, we assume it to be Hα, or [OII] if the emission line show a double peak profile. In these cases, the redshift was determined by fitting a Gaussian profile to the emission feature (a double Gaussian profile with a fixed separation was used for the [OII] doublet) and we report only the redshift solution (without the uncertainties). The

remaining 25 that could not be identified are listed in Table A.1 in the Appendix A.
We empirically estimated the uncertainties for the redshifts obtained with Redmonster (Hutchinson et al. 2016) by comparing the redshifts obtained for the same source in each individual exposure (see Section 2.3.1). We used a sub-sample of 25 sources for which Redmonster converged to a fit in at least 2 individual exposures (out of a total of 42 sources characterized with redshifts in the combined datacube), and studied the distribution of the differences between the redshifts obtained for each individual source. The dispersion in this distribution is due to the uncertainties of the redshift measurement in both exposures, and we determined its standard deviation to be $\sigma_{\rm diff}\approx 0.0002$. Therefore, assuming that both exposures have the same uncertainty, we can estimate an individual $\sigma_z \approx \frac{\sigma_{\rm diff}}{\sqrt{2}} \approx 0.00014$ for the Redmonster redshift measurements. Additionally, we looked for a cross-match between the SDSS spectroscopic catalog and our survey. We found 1 single source (the central QSO) to match, and the redshift difference was consistent with our estimated σ_z.

We classified sources with redshifts based on their spectral types as follows:

- Star-forming (*SF*): galaxies that show strong emission lines and a blue continuum. These 38 sources correspond to 73% of the sample with measured redshifts.

- Non-star-forming (*non-SF*): galaxies that show a strong red continuum and an absence of emission lines. These 6 sources correspond to ∼11% of the sample with measured redshifts.

- Red star-forming (*SF-red*): These galaxies show both a strong red continuum and emission lines consistent with recent star formation events. These sources are rare accounting for ∼6% of the sample with measured redshifts.

- QSO: We find a quasar-like spectrum for 3 sources, corresponding to ∼6% of the sample.

- Star: stellar-like spectrum. We identified a single star in our field.

- Lyα emitter candidate (LAE): One source showed a prominent single emission line, asymmetric and extended to the red, at a $\lambda \approx 5045$ Å. Given its observed wavelength, this can not be explained as an Hα emission. Furthermore, its profile and strength are inconsistent with this line being [OII]. Thus, we deem this source as a Lyα emitter candidate at z~3.15.

The distribution of sources in the field is shown in Fig. 3.2. For each source with a redshift we estimated the proper transverse distance to the QSO sight-line using our adopted Planck 2016 cosmology. We also calculated their absolute $r_{\rm AB}$ magnitude as follows:

$$M_{\rm r} = r_{\rm AB} - 5(\log(d_{\rm L}) - 1) - {\rm K_{corr}} \tag{3.1}$$

where $d_{\rm L}$ is the luminosity distance in parsecs. and $\rm K_{corr}$ is the corresponding K-correction for each galaxy (see Appendix B).

3.3 Survey characterization

In order to characterize the completeness of our survey we have used the apparent $r_{\rm AB}$ magnitudes. The left panel of Fig. 3.3 shows a histogram of sources per apparent $r_{\rm AB}$ magnitude bin, separating the sample for which good redshifts were obtained from the full sample. Our survey peaks at $r_{\rm AB} \approx 25$ mag. The sudden decline in the number of sources to fainter magnitudes marks our completeness limit. An apparent magnitude of $r_{\rm AB} = 25$ mag suggests a luminosity limit of $\sim 5 \times 10^8\,{\rm L_\odot}$ at $z \sim 0.5$. The central panel of the Fig. 3.3 shows the fraction of sources that were successfully assigned a redshift as a function of $r_{\rm AB}$ bin. Our characterization reaches $\sim 75\%$ for $r_{\rm AB} \approx 25$ mag. The right panel shows the redshift distribution of our full sample colored by spectral type.

Fig. 3.4 shows the distribution of impact parameter to the Q1410 sight-line as a function of redshift. The hatched area in the upper left corner shows the limit of the FoV of VLT/MUSE as a function of redshift; regions in the hatched area are out of the effective

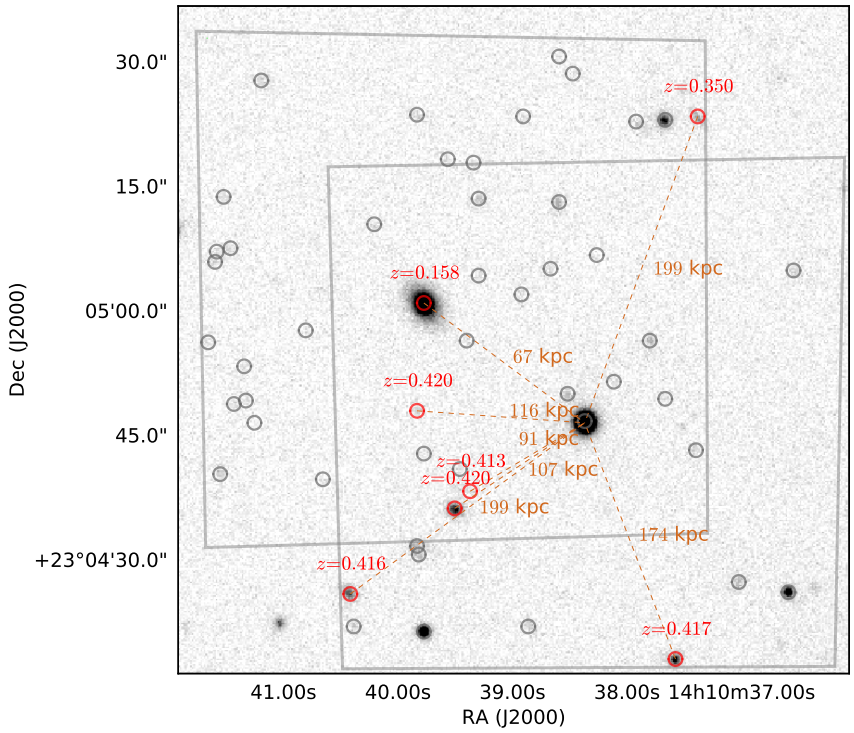

Figure 3.2: VLT/VIMOS image of our full MUSE field of view. The VLT/MUSE exposures are centered on the bright galaxy (upper left of the center) and the QSO Q1410 (lower right of the center) respectively (see Table 2.1). The gray contours mark the field of view of each individual VLT/MUSE exposure. We have characterized and measured redshifts for most sources brighter than $r = 25$ mag (see Tables 3.1 and 3.2)). Red circles show galaxies at redshifts within $\Delta v = \pm 1000$ km s^{-1} of any BLA. Grey circles mark the rest of the sources characterized with a redshift.

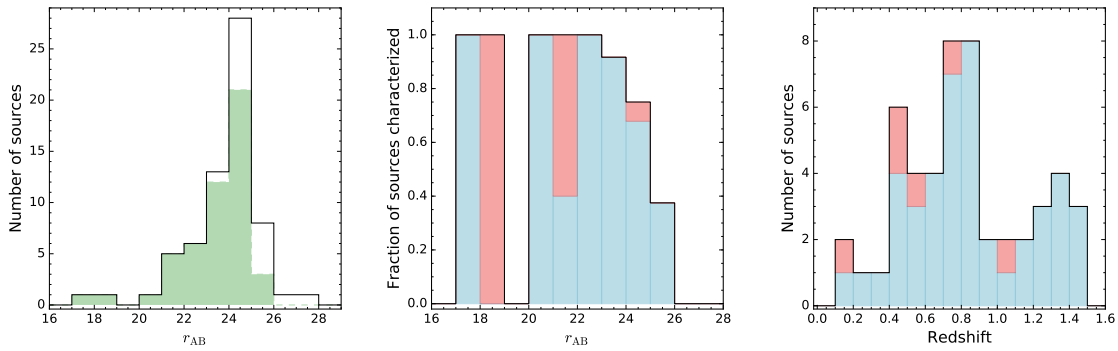

Figure 3.3: *Left*: Survey histogram colored in green for our sample with measured redshifts. The black line shows the distribution for the whole sample detected by SExtractor. Our detection threshold is at $r \sim 25$ mag. *Center* shows the completeness fraction of the redshift survey. The star forming galaxies are shown in blue and the non-star forming galaxies in red. The black contour marks our full sample. We reach to $\sim 75\%$ successful characterization fraction at an apparent magnitude $r_{\rm AB} = 25$ mag. *Right*: shows the redshift distribution of our full characterized sample colored by star forming and non-star forming fraction same as the central panel. The LAE candidate at $z \approx 3.15$ is not shown here.

VLT/MUSE coverage. At $z \approx 0.1$ our effective radial coverage is about 100 kpc, while at $z \approx 0.5$ we reach scales > 350 kpc. The vertical black lines mark the redshift of the inter-cluster axes reported by Tejos et al. (2016) that show a BLA. The vertical dashed regions around these lines represent a rest-frame velocity window of $\Delta v = \pm 1000\,\mathrm{km\ s^{-1}}$ around these redshifts. Excluding galaxies at the redshifts of the cluster-pairs, we found 9 sources brighter than apparent magnitude $r_{\rm AB} = 23$ mag. This represents a density of $22\,500 \pm 7\,500\,\mathrm{deg^{-2}}$, assuming a Poissonian error, which is consistent with the density of $\sim 20\,000\,\mathrm{deg^{-2}}$ found by the VVDS survey (Le Fèvre et al. 2005).

Tables 3.1 and 3.2 summarizes the characterization of the sources in our full survey.

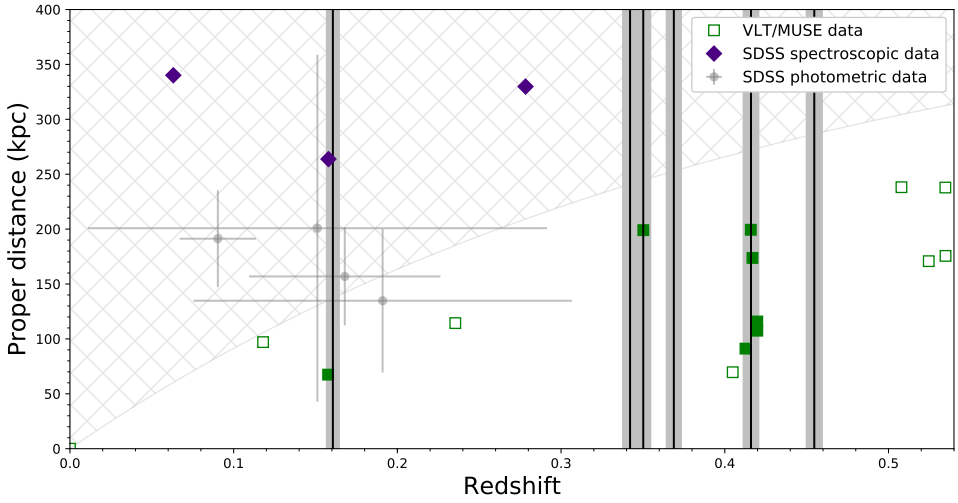

Figure 3.4: Distribution of impact parameter to the Q1410 sight-line as a function of redshift. Our VLT/MUSE sample of galaxies is shown in green squares. SDSS galaxies are shown in violet diamonds and gray circles (See Sect. 3.4 for details). We only show here galaxies in the SDSS photometric catalog that are outside the MUSE FoV. The vertical black lines surrounded by a shaded region mark the redshift of the inter-cluster axes ±1000 km s^{-1} from its rest frame. Filled squares mark sources in the VLT/MUSE sample that are located within ±1000 km s^{-1} of an inter-cluster axis and will be the subject of further analysis. The hatched area in the upper left corner is outside the MUSE FoV and shows the approximate edges of our spectroscopic survey.

Sources characterized in our survey

ID	Object	RA	DEC	Impact Parameter		r_{AB}	M_r	z	class	reliability
		J2000	J2000	(arcsecs)	(kpc)					
(1)	(2)	(3)	(4)	(5)	(6)	(7)	(8)	(9)	(10)	(11)
1	J141038.37+230446.5	212.65987	23.07958	0.0	0	17.35	-26.20	0.7961	QSO	a
2	J141038.52+230449.7	212.66050	23.08047	3.8	29	24.15	-22.08	0.7976	SF-red	a
3	J141038.11+230451.3	212.65879	23.08092	6.0	46	25.21	-19.31	0.7966	SF	c
4	J141037.66+230449.2	212.65692	23.08033	10.2	79	24.39	-18.75	0.8315	SF	a
5	J141037.80+230456.2	212.65750	23.08228	12.5	70	23.55	-19.20	0.4048	SF	b
6	J141037.40+230443.0	212.65583	23.07861	13.8	107	24.48	-19.91	0.7940	SF	b
7	J141039.46+230440.7	212.66442	23.07797	16.1	112	23.35	-19.55	0.6171	SF	a
8*	J141039.37+230438.1	212.66404	23.07725	16.2	91	24.77	-17.16	0.4126	SF	c
9	J141038.92+230501.8	212.66217	23.08383	17.1	137	24.82	-21.22	0.9093	SF	b
10	J141039.40+230456.2	212.66417	23.08228	17.2	149	24.94	-20.02	1.4865	SF	$b^{\perp}$
11	J141038.67+230504.8	212.66112	23.08467	18.8	136	24.37	-19.41	0.6750	SF	a
12*	J141039.50+230435.9	212.66458	23.07664	18.9	107	21.32	-21.29	0.4199	SF-red	a
13	J141039.77+230442.5	212.66571	23.07847	19.7	171	24.29	-19.55	1.4596	SF	$b^{\perp}$
14	J141038.27+230506.4	212.65946	23.08511	19.9	144	-	-	0.6676	SF	c
15*	J141039.84+230447.8	212.66600	23.07994	20.3	116	23.71	-18.83	0.4198	SF	a
16	J141039.29+230504.1	212.66371	23.08447	21.7	169	24.31	-146.55	3.1500	LAE	$c^{\perp}$
17*	J141039.77+230500.7	212.66571	23.08353	24.0	67	18.93	-20.94	0.1577	non-SF	a
18	J141039.83+230431.4	212.66596	23.07539	25.2	195	22.10	-22.41	0.8125	SF	a
19	J141038.86+230421.8	212.66192	23.07272	25.6	197	23.24	-21.14	0.7963	SF	b
20	J141039.82+230430.4	212.66592	23.07511	25.7	219	23.12	-20.73	1.2070	SF	$b^{\perp}$
21	J141038.60+230512.8	212.66083	23.08689	26.5	171	22.78	-20.43	0.5246	SF	a
22	J141037.02+230427.0	212.65425	23.07417	27.0	176	22.90	-19.99	0.5348	SF	a
23	J141039.29+230513.3	212.66371	23.08703	29.7	114	23.07	-17.71	0.2354	SF	a
24*	J141037.58+230417.9	212.65658	23.07164	30.6	174	21.96	-21.12	0.4169	non-SF	a
25	J141036.54+230504.7	212.65225	23.08464	31.1	269	23.92	-22.54	1.3583	SF	$b^{\perp}$
26	J141039.78+230421.1	212.66575	23.07253	32.0	256	20.44	-23.43	0.8975	QSO	b

Table 3.1: ($^{\perp}$): Redmonster did not converge to a z on these sources. Redshift were calculated by a visual inspection on these cases.

(*): Nearby Galaxies to the inter-cluster filaments. These sources are marked in red in Fig. 3.2. Source were classificated according to their spectral type. SF galaxies show strong emission lines and a blue continuum, non-SF galaxies show a strong red continuum and an absence of emission lines and SF-red galaxies show a strong red continuum and emission lines. We also identified a Lyα emitter candidate, which is classificated as LAE. Sources where r is undefined were not detected by SExtractor and we manually included them in this survey. The uncertainties of the Redmonster redshift measurements in the Col. (9) are of the order of ~0.00014.

Sources characterized in our survey

ID	Object	RA	DEC	Impact Parameter		r_{AB}	M_r	z	class	reliability
		J2000	J2000	(arcsecs)	(kpc)					
(1)	(2)	(3)	(4)	(5)	(6)	(7)	(8)	(9)	(10)	(11)
27	J141036.59+230425.9	212.65246	23.07386	32.1	277	21.13	-23.82	1.3400±0.00064	QSO	b
28	J141040.65+230439.5	212.66937	23.07764	32.2	278	25.69	-17.36	1.3118	SF	$b^{\perp}$
29	J141039.34+230517.6	212.66392	23.08822	33.9	289	23.69	-21.48	1.2081	SF	$c^{\perp}$
30	J141040.20+230510.2	212.66750	23.08617	34.6	300	24.32	-21.34	1.4305	SF	$b^{\perp}$
31*	J141040.42+230425.6	212.66842	23.07378	35.2	199	21.51	-21.26	0.4159±0.00004	non-SF	a
32	J141040.81+230457.3	212.67004	23.08258	35.4	289	99.00	53.56	0.9722±0.00012	SF	b
33	J141039.56+230518.1	212.66483	23.08836	35.6	308	24.44	-22.46	1.3849	SF	$b^{\perp}$
34	J141037.92+230522.5	212.65800	23.08958	36.5	238	22.41	-20.53	0.5347±0.00003	SF	a
35	J141040.38+230421.7	212.66825	23.07269	37.2	-	23.40	-	0.0000±0.00004	Star	a
36	J141038.91+230523.1	212.66212	23.08975	37.4	318	24.71	-21.80	1.1972±0.00008	SF	b
37	J141037.67+230522.8	212.65696	23.08967	37.6	238	21.44	-22.41	0.5079±0.00003	non-SF	a
38*	J141037.38+230523.1	212.65575	23.08975	39.1	199	22.39	-19.69	0.3502±0.00002	SF	a
39	J141041.26+230446.3	212.67192	23.07953	39.9	307	24.94	-27.97	0.7898±0.00049	non-SF	c
40	J141041.33+230448.9	212.67221	23.08025	40.9	327	24.78	-21.48	0.8960±0.00005	SF	a
41	J141041.34+230453.0	212.67225	23.08139	41.5	332	24.39	-27.77	0.8964±0.00017	SF	b
42	J141038.48+230528.4	212.66033	23.09122	41.9	325	24.95	-21.32	0.8123±0.00015	SF	c
43	J141039.83+230523.3	212.66596	23.08981	42.0	297	23.00	-20.95	0.6369±0.00004	SF	a
44	J141041.44+230448.6	212.67267	23.08017	42.4	340	25.09	-31.85	0.8979±0.00011	SF-red	a
45	J141038.59+230530.5	212.66079	23.09181	44.1	97	24.47	-14.58	0.1180±0.00017	SF	c
46	J141041.55+230440.1	212.67312	23.07781	44.3	339	23.35	-22.45	0.7741±0.00005	SF	a
47	J141041.66+230455.9	212.67358	23.08219	46.4	370	24.52	-31.97	0.8889±0.00024	SF	b
48	J141041.47+230507.3	212.67279	23.08536	47.6	406	24.01	-22.36	1.2077	SF	$b^{\perp}$
49	J141041.59+230505.7	212.67329	23.08492	48.4	358	23.84	-21.85	0.7086±0.00004	SF	a
50	J141041.58+230506.9	212.67325	23.08525	48.8	408	24.90	-24.02	1.0799±0.00011	SF	b
51	J141041.52+230513.5	212.67300	23.08708	51.2	428	24.71	-39.93	1.0793±0.00014	non-SF	a
52	J141041.19+230527.5	212.67162	23.09097	56.5	481	23.13	-22.36	1.1980±0.00004	SF	c

Table 3.2: ($^{\perp}$): Redmonster did not converge to a z on these sources. Redshift were calculated by a visual inspection on these cases.

(*): Nearby Galaxies to the inter-cluster filaments. These sources are marked in red in Fig. 3.2. Source were classificated according to their spectral type. SF galaxies show strong emission lines and a blue continuum, non-SF galaxies show a strong red continuum and an absence of emission lines and SF-red galaxies show a strong red continuum and emission lines. We also identified a Lyα emitter candidate, which is classificated as LAE. Sources where r is undefined were not detected by SExtractor and we manually included them in this survey. The uncertainties of the Redmonster redshift measurements in the Col. (9) are of the order of ~0.00014.

3.4 SDSS galaxies

As mentioned before, at low-z our VLT/MUSE survey has a relatively limited FoV. In particular, at $z \approx 0.16$ we would need to triplicate our current FoV to cover a physical impact parameter of ~ 300 kpc, which has been suggested for the so-called circum-galactic medium (CGM; Prochaska et al. 2011; Borthakur et al. 2016). In order to partially compensate this limitation, we have included galaxies with spectroscopic redshifts from the SDSS (SDSS Collaboration et al. 2016). These galaxies are marked with diamonds in Fig. 3.4. At $z \approx 0.16$ we found 3 SDSS galaxies, the closest being at an impact parameter of ~ 260 kpc to the QSO sightline. The remaining 2 are located at an impact parameter of >450 kpc and are not shown in Fig. 3.4 (See Table C.1). We have also looked for evidence of galaxies that we could be missing outside the MUSE FoV at the redshifts of the inter-cluster axis in the SDSS photometric catalog. We found ~400 additional galaxies closer than $4'$ around the line of sight, corresponding to a transverse distance of ~500 kpc at $z = 0.1$. Given the high uncertainties in the photometric redshifts (and consequently, in the estimated physical impact parameters), we have looked only for galaxies whose physical impact parameters may lie within 2 times their inferred virial radii to the QSO sightline, given their inferred stellar masses. Stellar masses were obtained from their photometry using the relation presented in Taylor et al. (2011). We then estimated their virial masses and virial radii in the same fashion as explained in Section 4.1 below. To be conservative, we considered the lower value of the error-bar for the physical impact parameter and the upper value of the error-bar for the virial radius (this uncertainty comes from the dispersion of ~0.1 dex in the stellar mass relation of Taylor et al. (2011)). We found 8 sources satisfying this condition between its impact parameter and virial radii at photometric redshifts $z < 0.5$, of which 4 are outside the MUSE FoV and are shown in Fig. 3.4 as gray circles (the other 4 were already detected by our MUSE spectroscopic survey). We found that 2 of these have photometric redshifts $z \lesssim 0.2$ with relatively low redshift uncertainties, making them unlikely to be associated to any of our BLAs at $z > 0.3$.

However, the remaining 2 need further analysis. Given that the uncertainties in the inferred proper impact parameter comes from the large uncertainty in the photometric redshift estimation, we can check if these galaxies could be related to the BLA at $z = 0.3422$ (or higher), by comparing their virial radius with the impact parameter that would have at that redshift. If we set these galaxies to be at that redshift, we obtain that their impact parameter would be higher than 4 times their estimated virial radius; if one of those galaxies is at z≈0.3422 (or higher), it would be at a large enough impact parameter for it not to be physically associated with the BLA. Thus, we conclude that we are likely not missing any galaxy outside the FoV of MUSE that could be directly associated to a BLA at redshift $z = 0.3422$ (or higher).

Chapter 4

Results

4.1 Galaxies at BLA redshifts

We now focus on galaxies that may be related to the BLAs of interest, i.e. those observed at redshifts of cluster-pairs as reported by Tejos et al. (2016). From our blind galaxy survey, we selected the subsample of galaxies lying within $\Delta v \pm 1000\,\mathrm{km\ s^{-1}}$ from any of the aforementioned BLAs. We found 7 out of the 52 characterized sources of the sample satisfying this criterion (filled green squares in Fig. 3.4), for which stellar masses, halo masses, virial radii and virial velocity dispersions were estimated. Stellar masses were calculated using the StarLight software (Cid Fernandes et al. 2005), which performs a spectral synthesis analysis assuming a Chabrier (2003) initial mass function (IMF). Since StarLight does not provide an estimation of the uncertainty for the inferred stellar masses, we assume its error to be 0.25 dex based on the analysis presented in Li et al. (2017, see their figure 1). Halo masses were estimated from the stellar masses by assuming the bijective relation between the two as given by Moster et al. (2010). We consider this inferred halo mass as a virial mass, M_{vir} of a galactic system and estimated a virial radius as,

$$R_{200} = \left(\frac{M_{\mathrm{vir}}}{\frac{4}{3}\pi 200 \rho_{\mathrm{c}}(z)} \right)^{1/3} \tag{4.1}$$

i.e., R_{200} is the radius of the spherical volume where $M_{\rm vir}$ is contained at 200 times the critical density of the Universe at a given redshift, $\rho_{\rm c}(z)$. Velocity dispersions for each galaxy were estimated as,

$$\sigma_{\rm vir} = \sqrt{\frac{GM_{\rm vir}}{R_{200}}} \tag{4.2}$$

Uncertainties in $M_{\rm vir}$, R_{200}, and $\sigma_{\rm vir}$ where estimated by propagating the adopted error in the stellar masses. Table 4.1 summarizes these inferred properties for our sample galaxies near BLAs.

In the following, we use the scales given by R_{200} and $\sigma_{\rm vir}$ of each galaxy to discriminate whether it could be directly associated to a BLA feature or not.

4.2 Potential association of galaxies to known BLAs

In Tejos et al. (2016) the authors identified 7 H I broad Lyα absorption features at 6 different redshifts, related to 6 out of the 7 inter-cluster axes at $0.1 < z < 0.5$. As seen in Fig. 3.4, 3 out of the 6 relevant inter-cluster axes show at least one nearby galaxy.[1]

In order to discriminate whether a BLA may be associated with one (or more) of these galaxies we consider both their impact parameters and their rest-frame absolute velocity difference $|\Delta v|$. We define $\eta = \frac{R_{\rm projected}}{R_{\rm vir}} \frac{|\Delta v|}{\sigma_{\rm vir}}$ (sometimes called caustic lines) to quantify the global environment. In Fig. 4.1, we show the impact parameter of each galaxy versus $|\Delta v|$ with respect to each BLA found at that redshift, in units of $R_{\rm vir}$ and $\sigma_{\rm vir}$ of the corresponding galaxy. Each galaxy-BLA pair is represented by a square coloured by the redshift of the galaxy given by the colour bar. In principle, if a BLA is close to a galaxy both in projection and velocity at values comparable to the $R_{\rm vir}$ and $\sigma_{\rm vir}$, respectively, it would indicate that the BLA may be have been produced by the galaxy halo rather than by the WHIM. $\eta < 2$ should mark the limit for a gravitationally bounded system (Shen et

[1]Note that there are 2 BLAs at $z \approx 0.416$, for which there is also a group of galaxies (see Table 4.2).

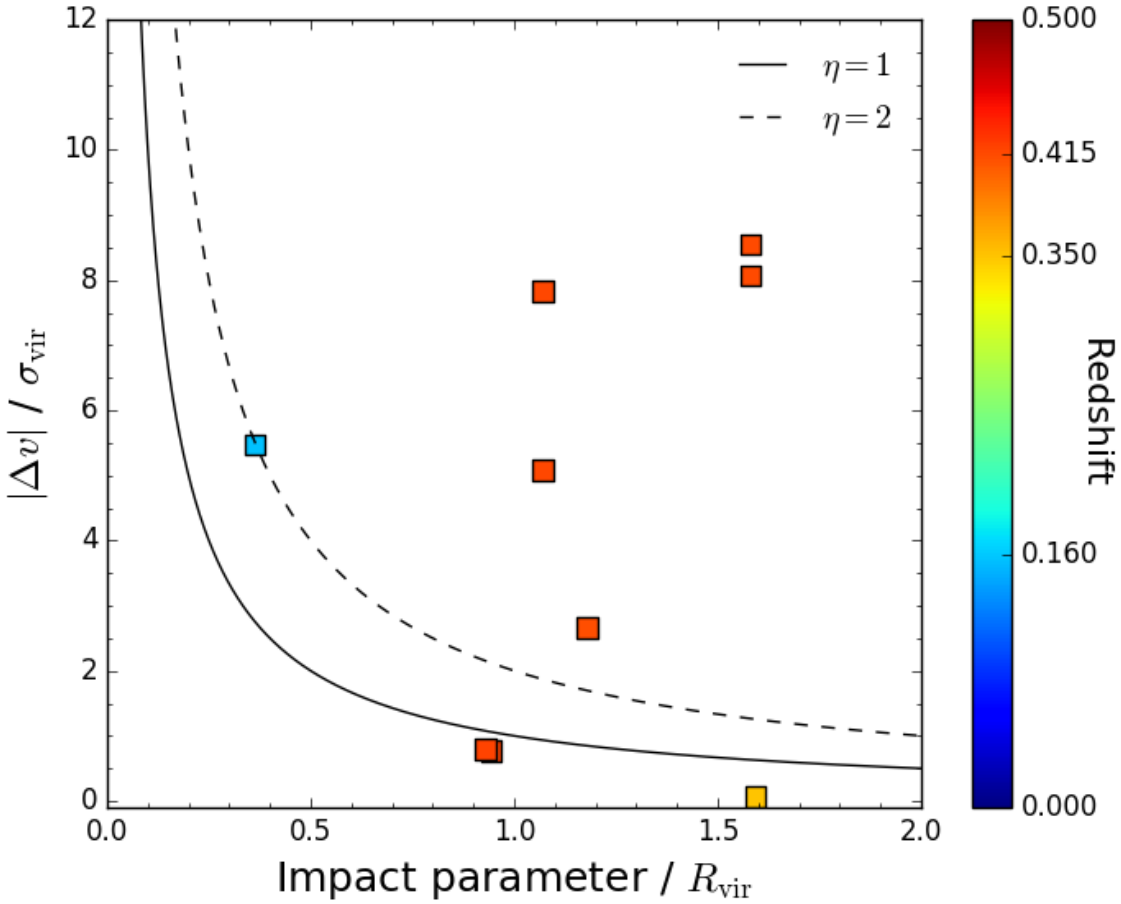

Figure 4.1: Each square represents a single galaxy-BLA combination identified from our sample, representing a total of 7 galaxies and 4 absorbers across three separate intra-cluster axes. The panel shows the relationship between potential host galaxies and absorbers in terms of a velocity difference and impact parameter to the QSO sight-line in units of $\sigma_{\rm vir}$ and $R_{\rm vir}$ respectively. The η is defined as $\frac{R_{\rm projected}}{R_{\rm vir}} \frac{|\Delta v|}{\sigma_{\rm vir}}$ and is used to quantify the global environment. $\eta < 2$ should mark the limit for a gravitationally bounded system (Shen et al. 2017).

Galaxies nearby known BLAs

ID	z	$M_{\rm vir}$	$R_{\rm vir}$	I.P.	$\sigma_{\rm vir}$	Δv
		$10^{11}{\rm M}_{\odot}$	kpc	kpc	km s^{-1}	km s^{-1}
(1)	(2)	(3)	(4)	(5)	(6)	(7)
1	0.1577	8.0±3.9	186±30	67	136±35	745
2	0.3502	3.0±1.0	125±14	199	102±18	-7
3	0.4126	0.8±0.2	77±7	91	65±10	-174
4	0.4159	3.4±1.2	126±14	199	107±20	-863
5	0.4169	7.2±3.3	162±24	173	138±33	700
6	0.4198	3.1±1.1	122±13	115	104±19	80
7	0.4199	2.6±0.9	115±12	107	98±17	78

Table 4.1: Galactic parameters of galaxies found to be close to the inter-cluster filaments. The Δv of each Galaxy respect to the nearby BLAs is shown in Fig. 4.2, where each galaxy is labeled according to their ID in this Table. Column (5) corresponds to the physical impact parameter of each galaxy to the Q1410 sight-line in kpc. Column (7) marks the Δv of the galaxy respect to the closest BLA in Fig. 4.2.

al. 2017, and references therein)[2]. For completeness, in Fig. 4.2 we show a portion of the Q1410 spectrum for each one of the inter-cluster axes that present a BLA on its rest-frame. Nearby galaxies are marked with arrows labeled with the IDs given in Table 4.1.

In the following, we give a brief description of each BLA system:

- The 2 BLAs at $z \approx 0.4160$ seems to be located in a galaxy group environment (with at least 5 galaxies). There are 2 galaxies at an impact parameter $\rho/R_{\rm vir} \sim 0.95$ and $|\Delta v|/\sigma_{\rm vir} \sim 0.7$, both below the $\eta = 1$ curve. Thus, we can not rule out that these BLAs may have been produced in the galaxy group halo (as opposed to WHIM).

[2]This limit were determined in the context of galaxy cluster physics, but we assume the same limit since the involved mechanisms are the same

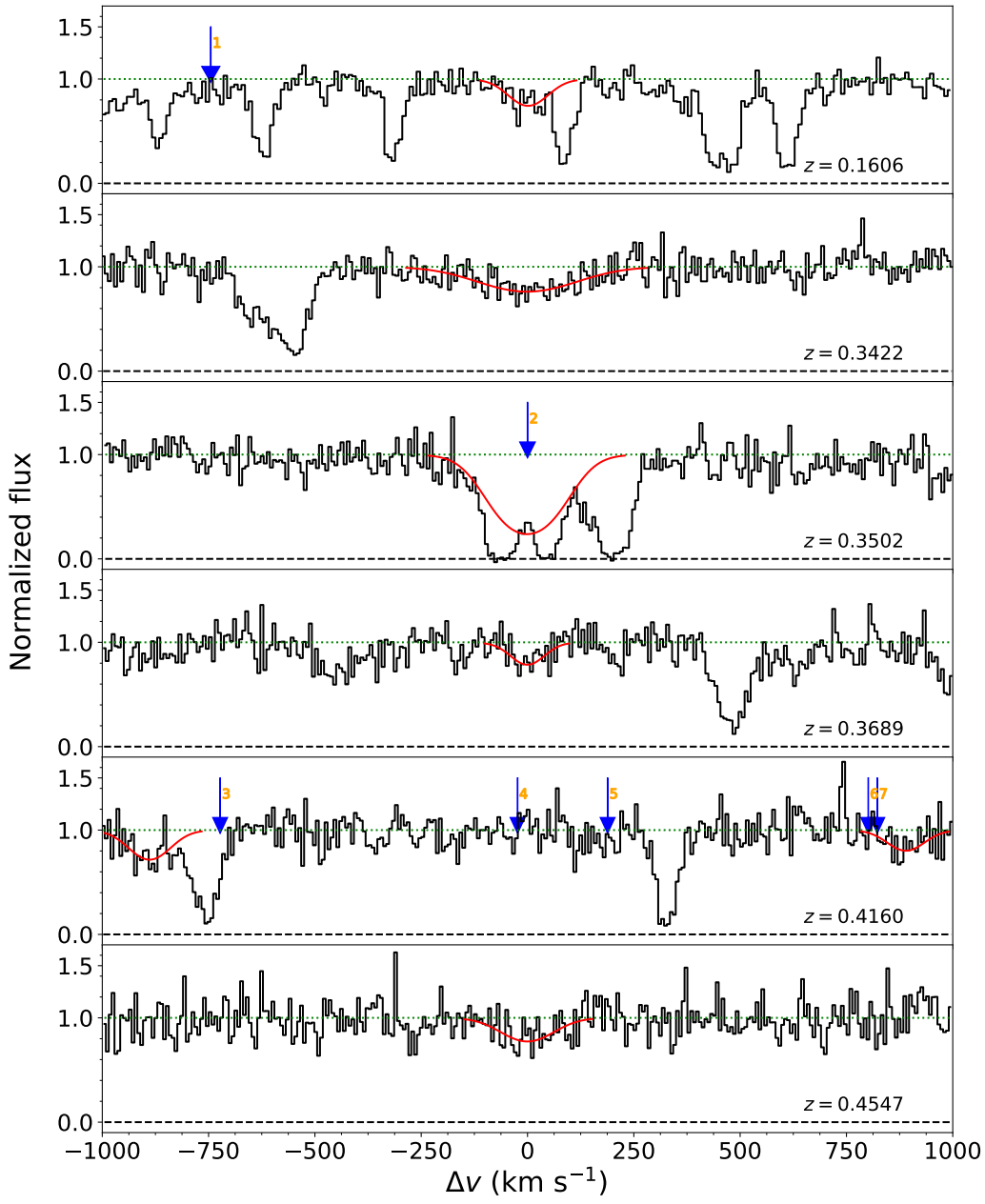

Figure 4.2: Panels show BLAs in the Q1410 COS spectrum within $\Delta v = \pm 1000$ km s^{-1} from the z of the inter-cluster axes. The panels are ordered by z. Arrows with numbers represent the redshifts of nearby galaxies, which are numbered according to Table 4.1 (Col. 1).

- The BLA at $z \approx 0.3502$ is very close to a strong narrow HI system that shows metal enriched gas (Tejos et al. 2016). It also has $|\Delta v|/\sigma_{\rm vir} < 0.5$ to the closest galaxy observed and it is located below the $\eta = 1$ curve. This places the absorption close to a galactic halo and its origin is uncertain. Moreover, our revised analysis of the absorption features in Q1410 (see Appendix E) deems this BLA as highly uncertain.

- The BLA at at $z \approx 0.1606$ has $\rho/R_{\rm vir} \sim 0.4$ but $|\Delta v|/\sigma_{\rm vir} \sim 5.4$. This places this BLA near the limit of $\eta = 2$. However, this latter BLA also shows a nearby galaxy from SDSS at an impact parameter of ≈ 260 kpc to the sight-line of the QSO with $|\Delta v| \approx 800\,{\rm km\ s^{-1}}$. Moreover, SDSS shows two more galaxies at higher impact parameters (~ 450 kpc), both at $|\Delta v| \sim 560\,{\rm km\ s^{-1}}$ (See Section 3.4).

- The BLAs at $z \approx 0.3422$, $z \approx 0.3689$, and $z \approx 0.4547$ do not show any potential host galaxy to a luminosity limit of $L \approx 4 \times 10^8\,{\rm L_\odot}$, corresponding to $\approx 0.01\,{\rm L_*}$ (Zucca et al. 2006; McNaught-Roberts et al. 2014) (or $\sim 3 \times 10^8 {\rm L_\odot}$ for $z \approx 0.3422$ and $\sim 5 \times 10^8 {\rm L_\odot}$ for $z \approx 0.4547$). We note that at those redshifts, our FoV cover impact parameters of ≈ 270, 280, and 320 kpc[3], respectively, comparable to the virial radius of an $\rm L_*$ galaxy. Still, as explained in Section 3.4, we have searched for photometric galaxies outside the MUSE FoV from the SDSS data, and found that the presence of such luminous galaxies right outside the FoV is unlikely.

As mentioned above, a detection limit of $r_{\rm AB} = 25$ mag implies a luminosity limit of $\sim 2-5\times10^8 {\rm L_\odot}$ at $z \approx 0.1-0.45$. We detected 7 galaxies brighter than this luminosity limit at the redshifts of the inter-cluster axes. We used a Schechter luminosity function to estimate the number of fainter galaxies that we could be missing given that we detected 7 galaxies brighter than the luminosity limit. We used $\alpha = -1.25$ and ${\rm L_*} = 3.15\times10^{10} {\rm L_\odot}$ (McNaught-Roberts et al. 2014) as the parameters for the luminosity function and ${\rm L_{min}} = 1 \times 10^6 {\rm L_\odot}$ (Sawala et al. 2016) as a conservative luminosity lower limit to integrate the luminosity function (although the existence of even fainter galaxies is possible such as fossils galaxies).

[3]These numbers may vary since our FoV is not symmetrically distributed around Q1410

From this, we estimate that < 1 faint galaxies may be missing. Thus, it is unlikely our analysis is significantly affected by an undetected population of faint galaxies.

Regarding large-scale structure, we remind the reader that we found evidence of a galaxy group in only 1 out of the seven inter-cluster axes probed by our MUSE survey (at $z \approx 0.461$). The lack of galaxy overdensities in the other 6, does not rule out the existence of a filamentary structure in them. According to the halo mass function presented in Reed et al. (2007), the average density of dark matter haloes more massive than $10^{12}\,h^{-1}\mathrm{M}_{\odot}$ is $0.004\,(h^{-1}\mathrm{Mpc})^3$. The volume sampled by MUSE inside the a single filament is about 400 kpc ×400 kpc ×6 Mpc. Considering an overdensity of factor ≈ 3 in the filaments with respect to the mean density of the Universe, and the fact that the sight-line passes through 7 independent inter-cluster axes, we would expect to detect ≈ 0.02 dark matter haloes more massive than $10^{12} M_{\odot}$ associated to the filaments in the MUSE FoV. This is consistent with what the single structure found in our data, within the Poissonian error.

4.3 Revision to the BLAs reported by Tejos et al. 2016

Given the intrinsic difficulty for finding and characterizing broad and shallow absorption features in QSO spectra, it is expected that some of the reported BLAs may be subject to large systematic uncertainties. In Appendix E we have performed independent analyses for quantifying potential systematic effects. We concluded that, with the exception of the putative BLA at $z = 0.3502$ (that could be even a narrow HI), all the other BLAs in inter-cluster axes reported by BLA have systematic uncertainties well below or consistent with the reported statistical uncertainties. Thus, given that the absorption feature at $z = 0.3502$ has already been discarded from our 'clean' sample of BLAs on the basis of the existence of a potential galaxy counterpart (see Section 4.2), we expect that the rest of the BLA sample is not much affected by systematic effect in the analysis of Tejos et al. (2016). In the following, we will use their reported fit parameters for these BLAs as these agree well with our new analyses within statistical uncertainties. We note that according to Tejos

et al. (2016), this sample of BLAs is complete down to a rest-frame equivalent width of $W_r = 0.039$ Å (see their figure 5). There are two BLAs in our sample that are close to this limit: the one at $z = 0.3689$ (with $W_r = 0.089 \pm 0.023$ Å) and the one at $z = 0.4202$ (with $W_r = 0.090 \pm 0.024$ Å). The latter is already discarded from our 'clean' sample because of the presence of a group of galaxies at a similar redshift, and we have opted to keep the former in.

In summary, our analyses indicate that 3 BLAs in inter-cluster axes do not show nearby potential host galaxy halos to stringent luminosity limits and their fit parameters are robust to tests on potential systematic effects (including data reduction, continuum estimation and Voigt profile fitting software). We consider these 3 BLAs to be good WHIM candidates. In the following, we will use their properties to assess the baryon content implied by these BLAs assuming these are genuine WHIM signatures. Note that another important concern regarding the BLAs characterization is the limited ability to disentangle blends. The importance of this systematic uncertainty depends on the S/N, as the higher the S/N, the easier it is to assess the kinematic structure of the absorption feature (e.g. Danforth et al. 2010; Richter et al. 2006). Although this is an intrinsic limitation of the absorption line technique, generally, one would expect an asymmetric profile for a blended line and this is not found on the BLAs in our sample. Also, the *full* characterization of the spectra of Q1410 performed in Tejos et al. (2016) (and not just restricted to the redshifts of the filaments) is crucial to minimize the misidentification of lines.

4.4 Density characterization of WHIM

For the three BLAs that do not show any nearby galaxy we can obtain the neutral hydrogen column density $N_{\rm HI}$ and the Doppler parameter b directly from the observed spectrum (Tejos et al. 2016). We split the observed Doppler parameter into two different components, thermal ($b_{\rm th}$) and non-thermal ($b_{\rm non-th}$),

$$b_{\rm obs} = \sqrt{b_{\rm th}^2 + b_{\rm non-th}^2} \tag{4.3}$$

The thermal broadening only depends on the temperature (T) of the gas,

$$b_{\rm th} = \sqrt{\frac{2k_bT}{m}} \approx 0.129\sqrt{\frac{T}{A}}{\rm km\,s^{-1}} \tag{4.4}$$

where k_b is the Boltzmann constant, m is the gas particle mass and A is the atomic weight of the element. For HI, equation 4.4 follows (e.g. Richter et al. 2006):

$$T \approx 60 \left(\frac{b_{\rm th}}{\rm km\,s^{-1}}\right)^2 {\rm K} \tag{4.5}$$

On the other hand, non-thermal broadening mechanisms include turbulence, Hubble flow, line blending, etc. In overdensities like inter-cluster filaments we may expect that turbulence dominates, and we parametrize it as being proportional to the thermal broadening, such that $b_{non-th} \approx b_{turb} \approx \alpha b_{th}$. This would imply:

$$b_{\rm obs}^2 \approx b_{\rm th}^2 + b_{\rm turb}^2 \approx b_{\rm th}^2(1+\alpha^2) \tag{4.6}$$

Cosmological hydrodynamical simulations from the OWLS project suggest $0 \leq \alpha \leq 1.3$ with a dependence on HI column density (Tepper-García et al. 2012, see their figure 5). If we restrict to absorption lines with column densities in the range of $10^{13} < N < 10^{14.5}\,{\rm cm^{-2}}$ these simulations suggest $\alpha \approx 0-0.8$. We also note that Richter et al. (2006) found values of $\alpha \approx 0.5$ from an independent simulation. Observationally, one could estimate α by comparing the observed Doppler parameters in systems with both HI and OVI, assuming they both come from the same gas in thermal equilibrium (Rauch et al. 1997). Savage et al. (2014) and Stocke et al. (2014) presented a sample with aligned[4] HI and OVI absorbers. Using the different line widths of both components, and given that the thermal Doppler broadening depends on the temperature and on the atomic mass (see Equation 4.4), they estimated the $b_{\rm non-th}$ contribution for each system. Considering only those systems where

[4] $\Delta v < 10$ km s^{-1} between the HI and OVI components

$b(\mathrm{HI})_{\mathrm{obs}} > 40$ km s^{-1} (18 out of their total sample) we studied the distribution for the α parameter in their sample. Their α values are distributed between $0.2 < \alpha < 2.1$, with an average of ≈ 0.7 where most of the values (15/18) have $\alpha < 1$.

Given that the BLAs in our sample do not show OVI, we can not empirically determinate the non-thermal broadening for our BLAs individually in this manner. Based on these theoretical and empirical studies, in the following we assume a fiducial value of $\alpha = 0.7$, but will leave its dependency explicit in the calculations. From equation 4.6 we then obtain the value of b_{th} given b_{obs}. Then we can estimate the temperature of the gas using equation 4.5.

In order to calculate the total gas column density, it is necessary to know the ionization fraction of the gas,

$$f_{\mathrm{ion}} \equiv \frac{N_{\mathrm{HI}} + N_{\mathrm{HII}}}{N_{\mathrm{HI}}} \approx \frac{N_{\mathrm{HII}}}{N_{\mathrm{HI}}} \tag{4.7}$$

i.e., the number of ionized hydrogen per neutral ones. If we take into account a pure collisional ionization equilibrium (CIE) scenario, f_{ion} depends only on the temperature of the gas and can be approximated by the polynomial (Sutherland & Dopita 1993):

$$\log(f_{\mathrm{ion}}) \approx -13.9 + 5.5\log\left(\frac{T}{\mathrm{K}}\right) - 0.33\log\left(\frac{T}{\mathrm{K}}\right)^2 \tag{4.8}$$

However, Richter et al. (2006) found that at the typical WHIM densities, photoionization from the UV background also contributes; neglecting it may underestimate the baryon density up to 50%. Their combined photoionization plus collisional ionization model suggests a linear relation between $\log(f_{\mathrm{ion}})$ and $\log(T)$ as

$$\log(f_{\mathrm{ion}}) \approx -0.75 + 1.25\log\left(\frac{T}{\mathrm{K}}\right) \tag{4.9}$$

for which f_{ion} as a function of b_{obs} and α can be written as:

$$f_{\mathrm{ion}} \approx 0.1778\left(\frac{T}{K}\right)^{1.25} \approx 29.7\left(\frac{b_{\mathrm{obs}}/\mathrm{km\,s^{-1}}}{\sqrt{1+\alpha^2}}\right)^{\frac{5}{2}} \tag{4.10}$$

Here we use equation 4.10 to infer $f_{\rm ion}$ and then calculate the total gas column density $N_{\rm H} \approx N_{\rm HII}$ for each individual BLA simply as $N_{\rm H} \approx f_{\rm ion} N_{\rm HI}$.

We assume a radial volumetric density profile for the inter-cluster filaments parametrized by an exponent Γ of the form

$$n_{\rm H}(r) = n_0 \frac{1}{1 + \left(\frac{r}{r_{1/2}}\right)^{\Gamma}} \tag{4.11}$$

where r is the radial distance to the filament axis (i.e. in cylindrical coordinates), n_0 is the peak density at filament center (except when Γ=0), and $r_{1/2}$ is a characteristic radius such that $n_H(r_{1/2}) = n_0/2$. Given this radial density profile we can solve

$$N_{\rm H} = \int n_{\rm H} dl \tag{4.12}$$

to estimate a mean particle density $\overline{n_{\rm H}}$ inside the filaments given our inferred $N_{\rm H}$. In the following, we use simple models based on two different values of Γ.

Uniform density model ($\Gamma = 0$)

The simplest case is a model in which the filament is a cylindrical structure with uniform density profile, i.e. $\Gamma = 0$ in 4.11. In this case,

$$N_{\rm H} = \int_0^L \frac{n_0}{2} dl \equiv \int_0^L \overline{n_{\rm H}} dl = \overline{n_{\rm H}} L \tag{4.13}$$

Thus $\overline{n_{\rm H}} = N_{\rm H}/L$ where L corresponds to the distance along the filament intersected by the QSO sight-line. As a first estimation, we can use the average diameter of the cosmic-web filaments of ≈ 6 Mpc as found by simulations (e.g González & Padilla 2010; Aragón-Calvo et al. 2010; Cautun et al. 2014). The true relation between L and the radius of the filament is uncertain, and it depends on the angle of incidence (θ) and the impact parameter relative to the radius of the filament ($\equiv \epsilon R$) of the sight-line to the center (e.g. see Figure 4.3 for an schematic). If $\theta \neq 0$ and $\epsilon = 0$, i.e. the sight-line is not perpendicular to the filament

but it passes through its center, $L = 2R/\cos(\theta)$. On the other hand, if $\theta = 0$ and $\epsilon \neq 0$, i.e. the sight-line is perpendicular to the filament but has an impact parameter of ϵR, $L = 2\sqrt{1-\epsilon^2}R$ (see Fig. 4.3). Thus, the mean density value for each BLA can be estimated as

$$\overline{n_{\rm H}} = \frac{N_{\rm H}}{L} = \frac{f_{\rm ion} N_{\rm HI} \cos(\theta)}{2\sqrt{1-\epsilon^2}R} \tag{4.14}$$

For simplicity, we assume a fiducial case where the sight-lines are all perpendicular and intersect the filaments at their centers. By averaging the $\overline{n_{\rm H}}$ for the three BLAs with no galaxies nearby we obtain

$$\langle\overline{n_{\rm H}}\rangle = 5.9{\times}10^{-6} \left(\frac{1-\epsilon^2}{1}\right)^{-\frac{1}{2}} \left(\frac{\cos(\theta)}{1}\right) \left(\frac{1+\alpha^2}{1.49}\right)^{-\frac{5}{4}} \text{cm}^{-3} \tag{4.15}$$

where we have left explicit the dependencies on our parameterizations.

4.4.1 Radial density profile model $\propto r^{-2}$ ($\Gamma = 2$)

As a more realistic approach, here we try a density profile for the inter-cluster filaments with a core and that follows $n_{\rm H}(r) \propto r^{-2}$ at large distances as suggested by simulations (e.g. Aragón-Calvo et al. 2010)

$$n_{\rm H} = n_0 \frac{1}{1 + \left(\frac{r}{r_{1/2}}\right)^2} \tag{4.16}$$

Assuming the same geometry as in the previous scenario, we integrate the density over a single sight-line to calculate the core density n_0

$$n_0 = \frac{N_{\rm H} \gamma \cos(\theta)}{2 r_{1/2}^2 \tan^{-1}(a/\gamma)} \tag{4.17}$$

where γ and a are geometrical parameters defined as follows

$$\gamma \equiv R\sqrt{\epsilon^2 + \left(\frac{r_{1/2}}{R}\right)^2} \tag{4.18}$$

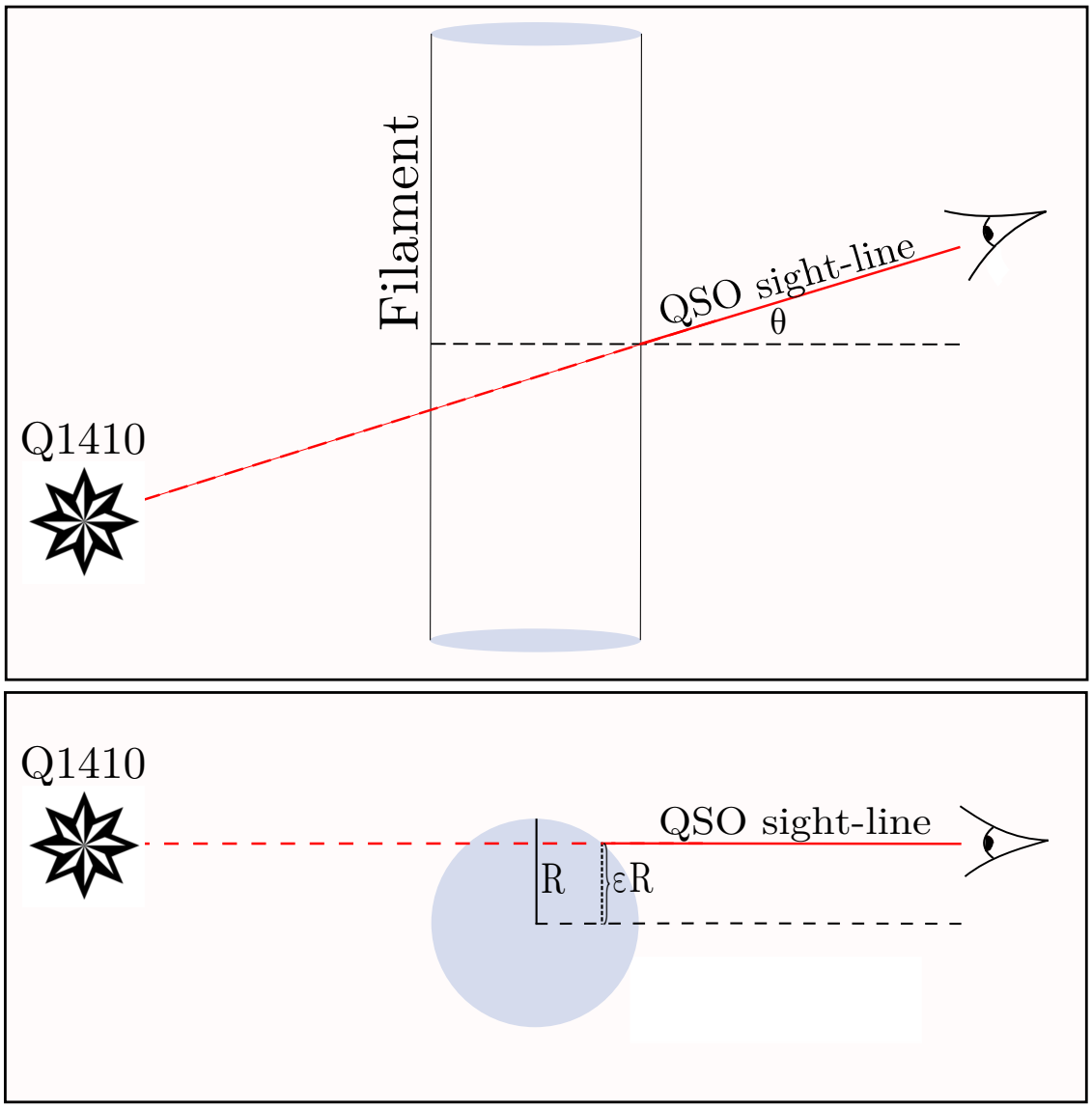

Figure 4.3: Schematic representation along the sight-line (in red) of the geometry assumed for deriving WHIM density. A filamentary structure is represented by a cylinder. θ is the angle between the sight-line and the perpendicular axis to the filament. The impact parameter of the sight-line respect to the center is parametrized by the fraction ϵ.

and

$$a \equiv R\sqrt{1-\epsilon^2} \tag{4.19}$$

and correspond to the typical size and typical core size of a filament. According to the results presented in Cautun et al. (2014), we use a value of $r_{1/2} = 2\,\mathrm{Mpc}$ and integrate the density profile until it becomes approximately flat, i.e. at $R \approx 6\,\mathrm{Mpc}$. Using the three good WHIM candidate BLAs in our sample, we can calculate a typical core density $\overline{n_0}$ and average the density profiles over the transversal area of the filament to obtain the averaged mean particle density:

$$\langle\overline{n_{\mathrm{H}}}\rangle = \overline{n_0}\int_A \frac{1}{1+(\frac{r}{r_{1/2}})^2}dA \tag{4.20}$$

From this, and using our fiducial values of $a = 6$ Mpc and $\gamma = 2$ Mpc we obtained a value of:

$$\overline{n_0} = 7.1{\times}10^{-6}\left(\frac{\tan^{-1}(a/\gamma)}{1.25}\right)^{-1}\left(\frac{\gamma}{2\,\mathrm{Mpc}}\right)\left(\frac{\cos(\theta)}{1}\right)\left(\frac{1+\alpha^2}{1.49}\right)^{-\frac{5}{4}}\mathrm{cm}^{-3} \tag{4.21}$$

for an average total integrated density of

$$\langle\overline{n_H}\rangle = 2.9{\times}10^{-6}\left(\frac{\tan^{-1}(a/\gamma)}{1.25}\right)^{-1}\left(\frac{\gamma}{2\,\mathrm{Mpc}}\right)\left(\frac{\cos(\theta)}{1}\right)\left(\frac{1+\alpha^2}{1.49}\right)^{-\frac{5}{4}}\mathrm{cm}^{-3} \tag{4.22}$$

Table 4.2 summarizes the main findings adopting our fiducial values for the individual WHIM candidate BLAs. For completeness, in Table 4.2 we have also included the corresponding calculations for those BLAs that show nearby galaxies (marked with 'y' in the last column). Note that for the latter, the presence of nearby galaxies complicates the interpretation on its origin but does not necessarily rule out the possibility that these are genuine WHIM absorption. In fact we do not see an important quantitative difference in the inferred densities for good and uncertain WHIM candidates. We obtained a mean hydrogen particle density of $5.9{\pm}4.1{\times}10^{-6}\,\mathrm{cm}^{-3}$ in the uniform density scenario (Sect. 4.4) using the samples of BLAs that do not show nearby galaxies. If we use only the BLAs

Parameters derived from BLAs

ID	Redshift	b	Column densities		$\log f_{\rm ion}$	Temperature	Gas density		Has galaxy
							$\Gamma = 0$	$\Gamma = 2$	nearby?
		km s^{-1}	$\log(N_{\rm HI}/{\rm cm}^{-2})$	$\log(N_{\rm HII}/{\rm cm}^{-2})$		$\log(T/{\rm K})$	$\log(\overline{n_{\rm H}}/{\rm cm}^{-3})$		
(1)	(2)	(3)	(4)	(5)	(6)	(7)	(8)	(9)	(10)
1	0.1606	59±22	13.40±0.11	19.1±0.4	5.68±0.40	5.1±0.3	-6.2±0.4	-6.5±0.4	y
2	0.3422	153±19	13.75±0.05	20.5±0.1	6.72±0.13	6.0±0.1	-4.8±0.1	-5.1±0.1	n
3	0.3502	97±10	14.29±0.09	20.5±0.1	6.22±0.11	5.6±0.1	-4.8±0.1	-5.1±0.1	y
4	0.3689	50±18	13.25±0.11	18.8±0.4	5.50±0.39	5.0±0.3	-6.5±0.4	-6.8±0.4	n
5	0.4118	62±18	13.47±0.09	19.2±0.3	5.74±0.32	5.2±0.3	-6.1±0.3	-6.4±0.3	y
6	0.4202	56±20	13.25±0.12	18.9±0.4	5.63±0.39	5.1±0.3	-6.4±0.4	-6.7±0.4	y
7	0.4547	81±18	13.46±0.08	19.5±0.3	6.03±0.24	5.4±0.2	-5.8±0.3	-6.1±0.3	n

Table 4.2: Characterization of each BLA. The errors associated to the redshifts in the column (2) are $\sim\pm10$ km s^{-1}. The mean density $\overline{n_{\rm H}}$ was calculated for both scenarios proposed in Sect. 4.4 for all BLAs. Column (10) marks as 'n' the absorptions that are likely produced by WHIM according to Sect. 4.2

that could be potentially associated with a galaxy, we obtain a mean particle density of $4.9 \pm 4.2 \times 10^{-6}\,{\rm cm}^{-3}$. Similarly, in the radial density profile scenario we obtained a mean particle density of $2.9 \pm 2.0 \times 10^{-6}\,{\rm cm}^{-3}$ (Sect. 4.4.1). If we consider now the BLAs with uncertain origin only, we obtain a value of $2.4 \pm 2.1 \times 10^{-6}\,{\rm cm}^{-3}$.

Chapter 5

Discussion

5.1 The relation between BLAs and WHIM

Based on our blind MUSE survey, we have a first estimation of the fraction of BLAs in inter-cluster filaments that may represent genuine WHIM signatures based on the lack of nearby galaxies to stringent luminosity limits. We find this fraction to be ∼40% (3/7). Despite an analysis of the luminosity function, we cannot rule out the presence of fainter or dust-enshrouded galaxies.

How this number relates to BLAs discovered in blind absorption surveys is particularly relevant for observational studies focused on the WHIM. Although properly addressing this question is beyond the scope of this thesis, we note that one could repeat the experiment presented here in non-targeted QSO sight-lines and undertake an empirical comparison.

5.2 The baryon density in inter-cluster filaments

Here we provide an estimation of the implied baryon density in inter-cluster filaments, $\Omega_{\rm b}^{\rm fil}$. The results presented in Section 4.4 correspond to the typical volumetric densities implied by our 3 BLAs that are good WHIM candidates. In order to estimate the corresponding baryon density, we need to estimate the relative volume occupied by these

large-scale filaments in the Universe $V_{\rm fil}$. Thus,:

$$\Omega_{\rm b}^{\rm fil} = \frac{8\pi G m_{\rm H}}{3H(z)^2(1-Y)} \langle \overline{n_{\rm H}} \rangle V_{\rm fil} \tag{5.1}$$

where G is the gravitational constant, $m_{\rm H}$ is the hydrogen mass, $H(z)$ is the Hubble parameter, and Y is the baryonic mass fraction in Helium. In the following we use a typical volume $V_{\rm fil} \sim 6\%$ as inferred by cosmological simulations (e.g. Cautun et al. 2014). We note that this volume fraction may not be consistent with a uniform density model, given that such number comes from simulations with a non-uniform density profile. Nevertheless, we have kept this number fixed as a fiducial value, but our results will be expressed explicitly on $V_{\rm fil}$.

5.2.1 Uniform density model

In the scenario of filaments with uniform density (see Sect. 4.4), assuming θ=0, ϵ=0 and $\alpha = 0.7$ as fiducial values, we estimated a mean gas particle density of $\langle \overline{n_{\rm H}} \rangle \approx 5.9{\times}10^{-6}$ cm^{-3}. According to equations 4.15 and 5.1 we have

$$\Omega_{\rm b}^{\rm fil} \approx 0.06 \left(\frac{\langle \overline{n_{\rm H}} \rangle}{5.9x10^{-6}{\rm cm}^{-3}} \right) \left(\frac{V_{\rm fil}}{0.06} \right) \left(\frac{1-Y}{0.76} \right)^{-1} \tag{5.2}$$

giving us a value of $\Omega_{\rm b}^{\rm fil} \approx 0.06 \pm 0.04$, i.e. somewhat larger than the total baryon density expected $\Omega_{\rm bar} \approx 0.048$ (e.g. Planck Collaboration et al. 2016) but consistent within the errors. The error in this estimations comes from the standard error of the mean density of our sample. With the aim at reducing the statistical uncertainties, here we also include the densities of the BLAs reported in Wakker et al. (2015). The authors reported a total of 5 BLAs, 4 of them in sight-lines within 540 kpc to the axis of the filament and 1 of them at an impact parameter of ~ 3 Mpc. We added these 5 BLAs to our sample, and calculated the corresponding $\langle \overline{n_{\rm H}} \rangle$ in the same manner as in Sect. 4.4.[1] Combining their and our sample of BLAs we obtain a somewhat better constrained value of $\Omega_{\rm b}^{\rm fil} \approx 0.04 \pm 0.02$.

[1]We note that the BLAs reported in Wakker et al. (2015) arise from the same filamentary structure instead of independent ones.

5.2.2 Radial density model $\propto r^{-2}$

Alternatively, in the scenario of a density profile $\propto r^{-2}$ (see Section 4.4.1) and using the same fiducial values for the main parameters as in the previous section, we estimated a mean gas peak density of $\overline{n_0}$=7.1×10^{-6} cm^{-3}. By averaging the density profile over the transversal area of the filament, we obtained an overall mean gas particle density of $\langle\overline{n_{\rm H}}\rangle$=2.9×10^{-6} cm^{-3}. Using equations 4.22 and 5.1 we obtain an alternative value for $\Omega_{\rm b}^{\rm fil}$ as

$$\Omega_{\rm b}^{\rm fil} \approx 0.03 \left(\frac{\langle\overline{n_{\rm H}}\rangle}{2.9x10^{-6}{\rm cm}^{-3}}\right)\left(\frac{V_{\rm fil}}{0.06}\right)\left(\frac{1-Y}{0.76}\right)^{-1} \tag{5.3}$$

This new fiducial value $\Omega_{\rm b}^{\rm fil} \approx 0.03 \pm 0.02$ is somewhat lower than $\Omega_{\rm bar} \approx 0.048$, but subject to large statistical and systematic uncertainties. If we include in our sample the BLAs reported in Wakker et al. (2015) (see Section 5.2.1) we obtain a somewhat better constrained value of $\Omega_{\rm b}^{\rm fil} \approx 0.02 \pm 0.01$, consistent with expected value of $0.4 \times \Omega_{\rm bar} \approx 0.02$.

Chapter 6

Summary and Conclusions

In this thesis we used VLT/MUSE to perform a blind galaxy survey around a unique QSO whose sightline may be passing through 7 inter-cluster filaments as presented in Tejos et al. (2016). In particular, we focus on the presence or lack of galaxies within $\Delta v = \pm 1000\,\mathrm{km\ s^{-1}}$ from each of the 7 broad HI Lyα absorption (BLAs) found at these inter-cluster redshifts in order to determine their origin.

We detected 77 sources and characterized the redshift of 52 of them. We reached 100% characterization completeness down to magnitude $r = 23$ mag, and $\approx 75\%$ completeness down to magnitude $r = 25$ mag. We found that 4 of the BLAs showed nearby galaxies, for which the origin of the BLAs is uncertain. These include a galaxy group at $z \approx 0.416$ and a potential galaxy halo BLA at $z \approx 0.35$ (not well constrained by the data, see Appendix E). On the other hand, we found 3 BLAs that do not show any galaxy nearby to stringent luminosity limits. The lack of a nearby galaxy implies that they may be produced by the long sought after warm-hot intergalactic medium (WHIM), and would mean that a significant fraction ($\sim$ 40%) of the BLAs detected between cluster-pairs (where the existence of a filamentary structure can be expected), may be directly tracing WHIM.

Assuming these BLAs are genuinely produced by the WHIM, we estimated the mean gas

particle density assuming two different density profile models for the filaments themselves. First, we used an uniform density profile scenario with a set of assumptions on the geometry and the broadening mechanisms involved, and estimated a rough mean gas density of $\langle\overline{n_H}\rangle \sim (5.9 \pm 4.1) \times 10^{-6}$ cm^{-3}. This value implies an unrealistically large $\Omega_{\rm bar}^{\rm fil} \approx 0.06 \pm 0.04$,i.e. larger than the expected total baryon density of $\Omega_{\rm bar} \approx 0.048$ (Planck Collaboration et al. 2016) but still consistent within errors. In the second scenario, we assumed a radial density profile of the form $n_{\rm H}(r) \propto r^{-2}$ (as suggested by simulations; e.g. Aragón-Calvo et al. 2010), which led us to estimate a mean gas particle density of $\langle\overline{n_{\rm H}}\rangle \sim (2.9 \pm 2.0) \times 10^{-6}$ cm^{-3} and a corresponding $\Omega_{\rm bar}^{\rm fil} \approx 0.03 \pm 0.02$. This value is similar to the expected $0.4\Omega_{\rm bar} \approx 0.02$ that may be in a WHIM state. Including the BLAs presented in Wakker et al. (2015) into our sample we obtain somewhat better constrained values for $\Omega_{\rm bar}^{\rm fil}$ of 0.04 ± 0.02 and 0.02 ± 0.01 for the uniform density and radial density model, respectively.

We emphasize that these estimations are subject to large statistical and systematic uncertainties, owing to our small sample of BLAs (3 and 3 + 5) and to the intrinsic uncertainties of our assumed geometrical parameters. Furthermore, the relationship between observed Doppler b parameters and gas-phase temperature is affected by poorly-constrained physical processes (e.g. turbulence). The results presented here support the hypothesis that inter-cluster filaments host a significant amount of baryons, enough to close the baryon budget in the low-z Universe but larger samples need to be analyzed for conclusive results.

Acknowledments

Our results are based on observations collected at the European Organisation for Astronomical Research in the Southern Hemisphere under ESO programme 094.A-0575(C). Some of the data presented in this thesis were obtained from the NASA/ESA Hubble Space Telescope under programme GO 12958, obtained at the Space Telescope Science Institute and from the Mikulski Archive for Space Telescopes (MAST). STScI is operated by the Association of Universities for Research in Astronomy, Inc., under NASA contract NAS5-26555. I.P. and N.T. acknowledge support from *CONICYT PAI/82140055.*

We thank contributors to SciPy, Matplotlib, Astropy (Astropy Collaboration et al. 2013) and the PYTHON programming language; the free and open-source community; and the NASA Astrophysics Data System for software and services. We also thank contributors to linetools (Prochaska et al. 2016) and PyMUSE (Pessa et al. 2018), both open-source PYTHON packages recently developed and used in this work.

Appendix A

Uncharacterized sources

Table A.1 lists photometric sources identified in the MUSE dataset but for which no redshift solution was found.

Sources not characterized in our survey

ID	Object	RA J2000	DEC J2000	Impact Parameter (arcsecs)	r_{AB}	reliability
(1)	(2)	(3)	(4)	(5)	(6)	(7)
1	J141038.12+230441.3	212.65883	23.07814	6.24	-	d
2	J141038.57+230440.7	212.66071	23.07797	6.42	24.27	d
3	J141038.54+230453.0	212.66058	23.08139	6.91	24.79	d
4	J141038.17+230435.9	212.65904	23.07664	10.95	25.36	d
5	J141037.60+230443.3	212.65667	23.07869	11.10	-	d
6	J141037.51+230445.8	212.65629	23.07939	11.89	24.57	d
7	J141039.24+230453.5	212.66350	23.08153	13.90	-	d
8	J141039.15+230456.4	212.66312	23.08233	14.62	-	d
9	J141038.38+230430.3	212.65992	23.07508	16.20	-	d
10	J141039.03+230430.7	212.66262	23.07519	18.24	24.21	d
11	J141038.55+230425.6	212.66062	23.07378	21.05	24.69	d
12	J141039.98+230454.5	212.66658	23.08181	23.61	-	d
13	J141037.24+230505.8	212.65517	23.08494	24.81	25.57	d
14	J141039.87+230425.6	212.66612	23.07378	29.42	27.38	d
15	J141036.36+230426.5	212.65150	23.07403	34.20	23.96	d
16	J141036.33+230507.5	212.65137	23.08542	35.12	-	d
17	J141036.65+230419.5	212.65271	23.07208	35.95	-	d
18	J141040.73+230508.3	212.66971	23.08564	39.19	24.96	d
19	J141038.38+230526.0	212.65992	23.09056	39.50	-	d
20	J141036.28+230418.2	212.65117	23.07172	40.41	-	d
21	J141041.09+230503.6	212.67121	23.08433	41.25	25.22	d
22	J141040.93+230508.3	212.67054	23.08564	41.51	26.30	d
23	J141037.52+230526.5	212.65633	23.09069	41.68	25.27	d
24	J141041.61+230437.6	212.67337	23.07711	45.59	25.17	d
25	J141039.53+230532.5	212.66471	23.09236	48.71	24.06	d

Table A.1: List of the sources that could not be characterized. Sources where r is undefined were not detected by SExtractor and we manually included them in the survey.

Appendix B

K-correction

We have calculated the photometric K-correction in the r filter for galaxies in our survey as follows. We used empirical templates presented in Coleman et al. (1980) extended to blue wavelengths according to Bruzual & Charlot (2003) models to calculate the predicted $r - i$ color and observed $r_{\rm AB}$ at different redshifts for different spectral types from E to Im. We obtained a monotonic relation between $r - i$ color and K-correction for each redshift bin. We then empirically calculated the $r - i$ color for the galaxies in our survey with known redshifts and interpolated this relation to obtain their corresponding K-correction.

Appendix C

SDSS galaxies

Table C.1 lists SDSS spectroscopic galaxies from the SDSS outside our MUSE FoV up to impact parameters of ≈500 kpc.

SDSS galaxies

Object		r	Impact parameter	z
RA	DEC		kpc	
14:10:33.00	+23:05:44.87	17.04	264	0.1579
14:10:46.43	+23:02:49.87	17.12	456	0.1584
14:10:50.97	+23:05:13.20	16.72	494	0.1580

Table C.1: List of the SDSS galaxies found to be close to z∼0.16

Appendix D

Redmonster redshifts measurements

Figs. D.1, D.2, D.3, D.4, D.5, D.6 and D.7 shows the spectra of identified sources in the MUSE data that were characterized using Redmonster software.

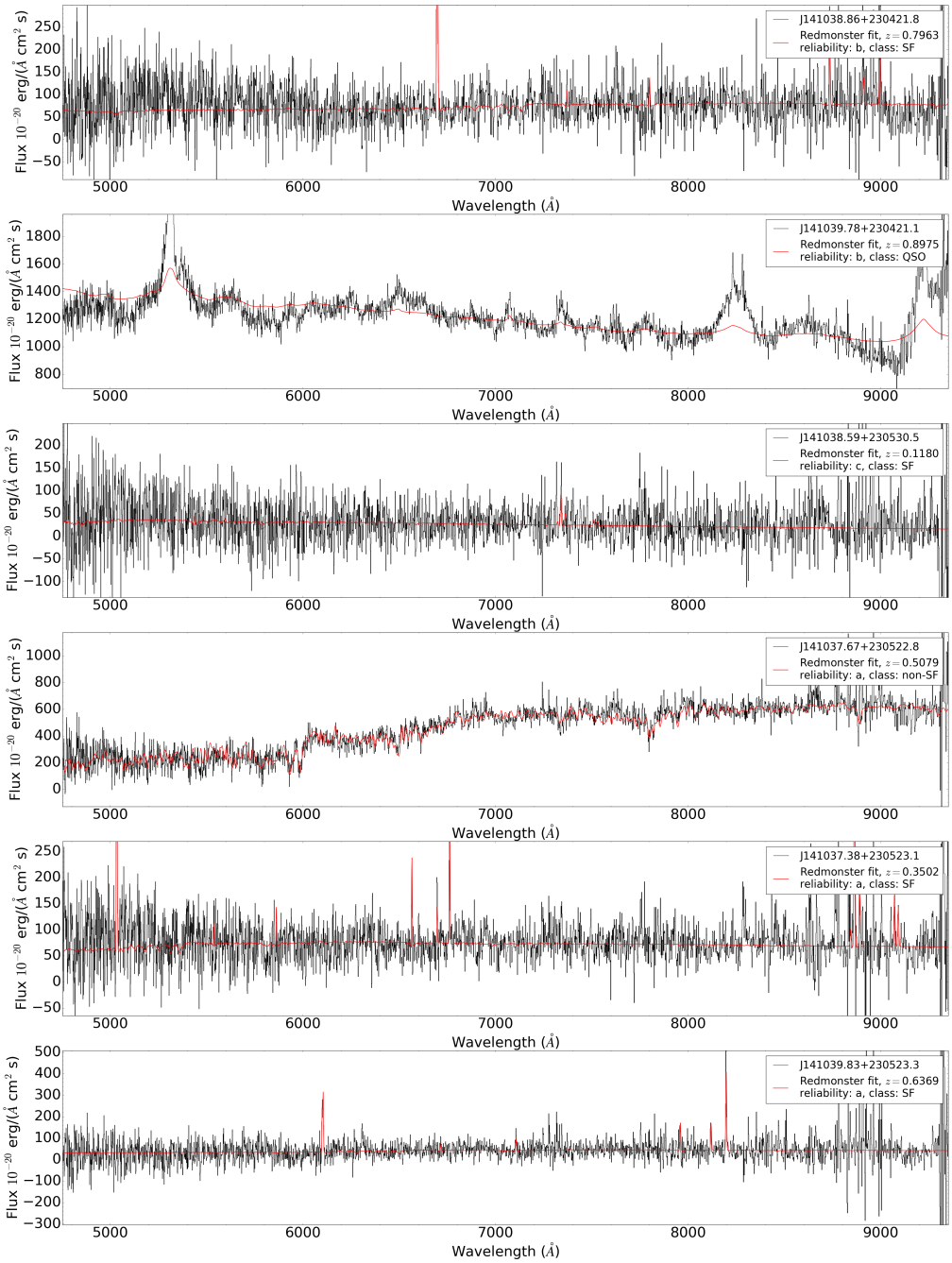

Figure D.1: Spectra characterized using Redmonster software

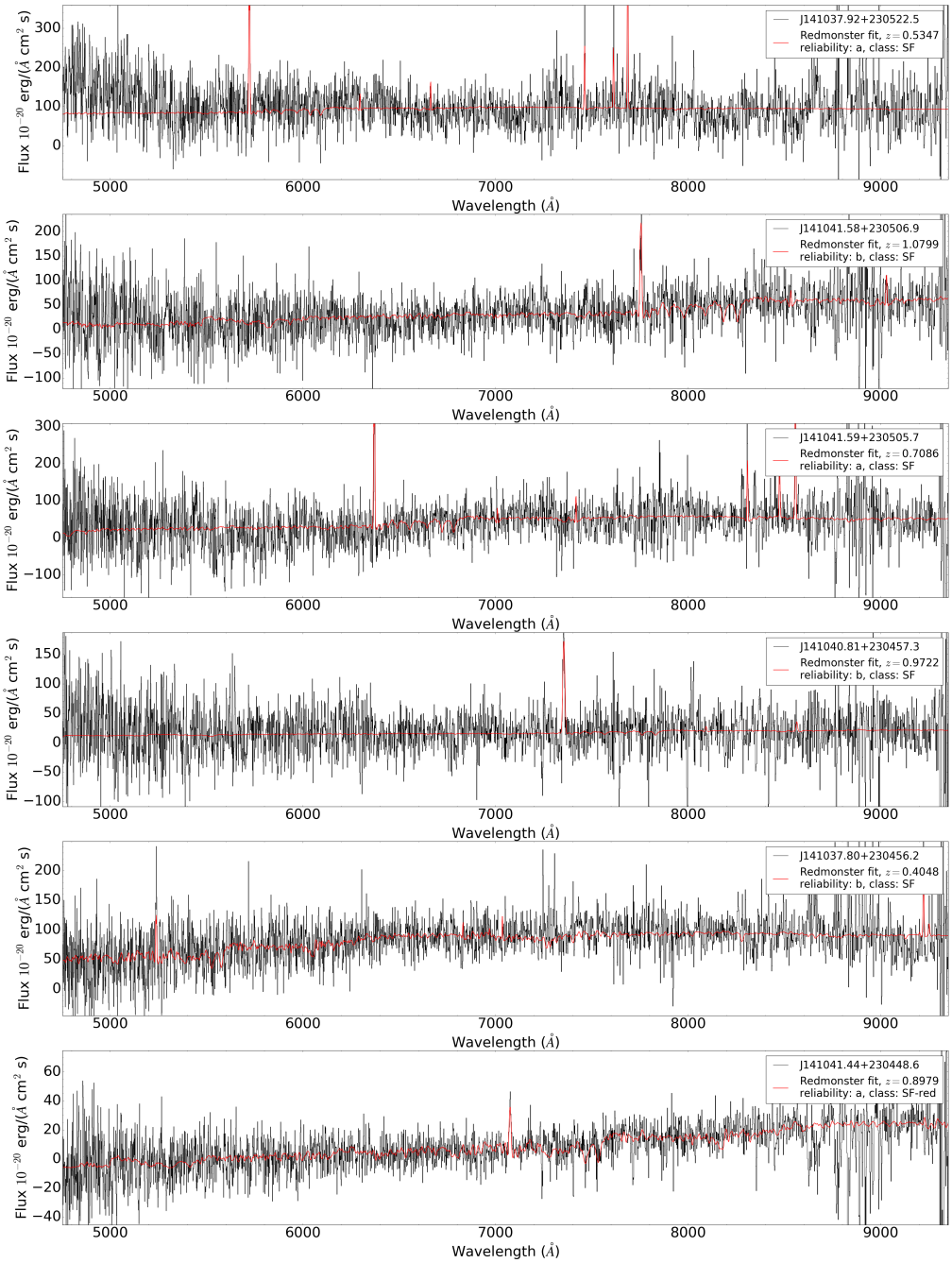

Figure D.2: Spectra characterized using Redmonster software

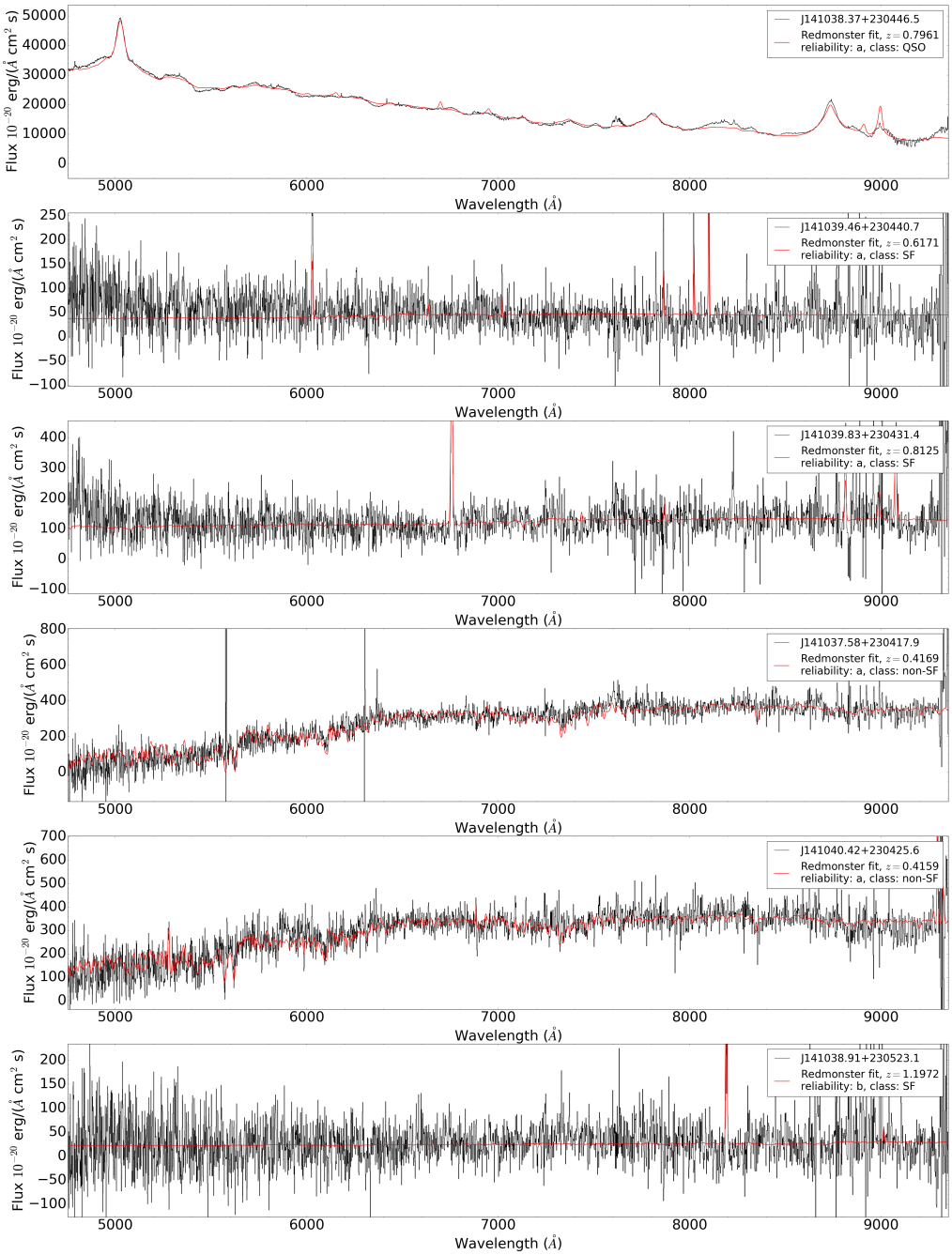

Figure D.3: Spectra characterized using Redmonster software

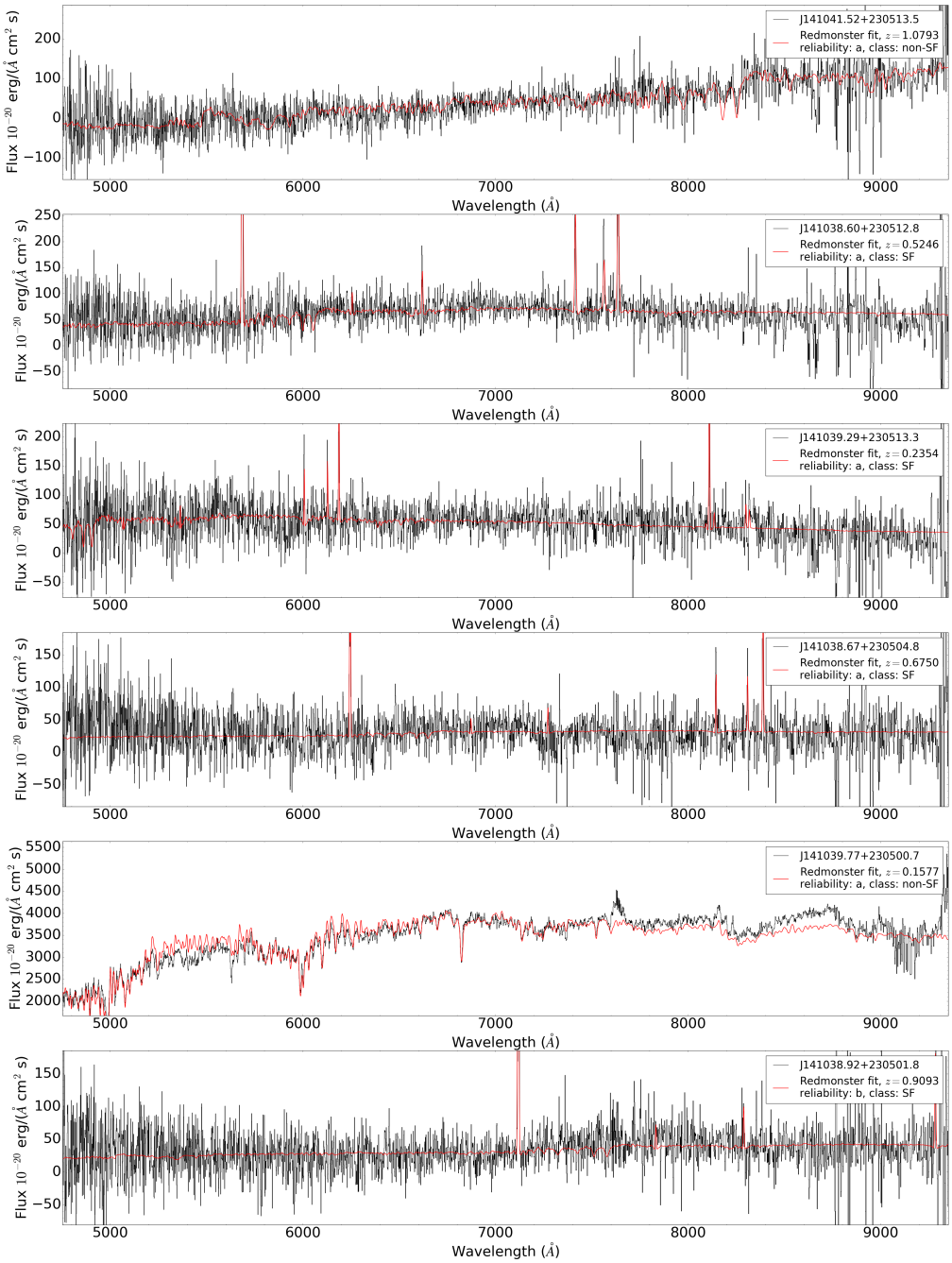

Figure D.4: Spectra characterized using Redmonster software

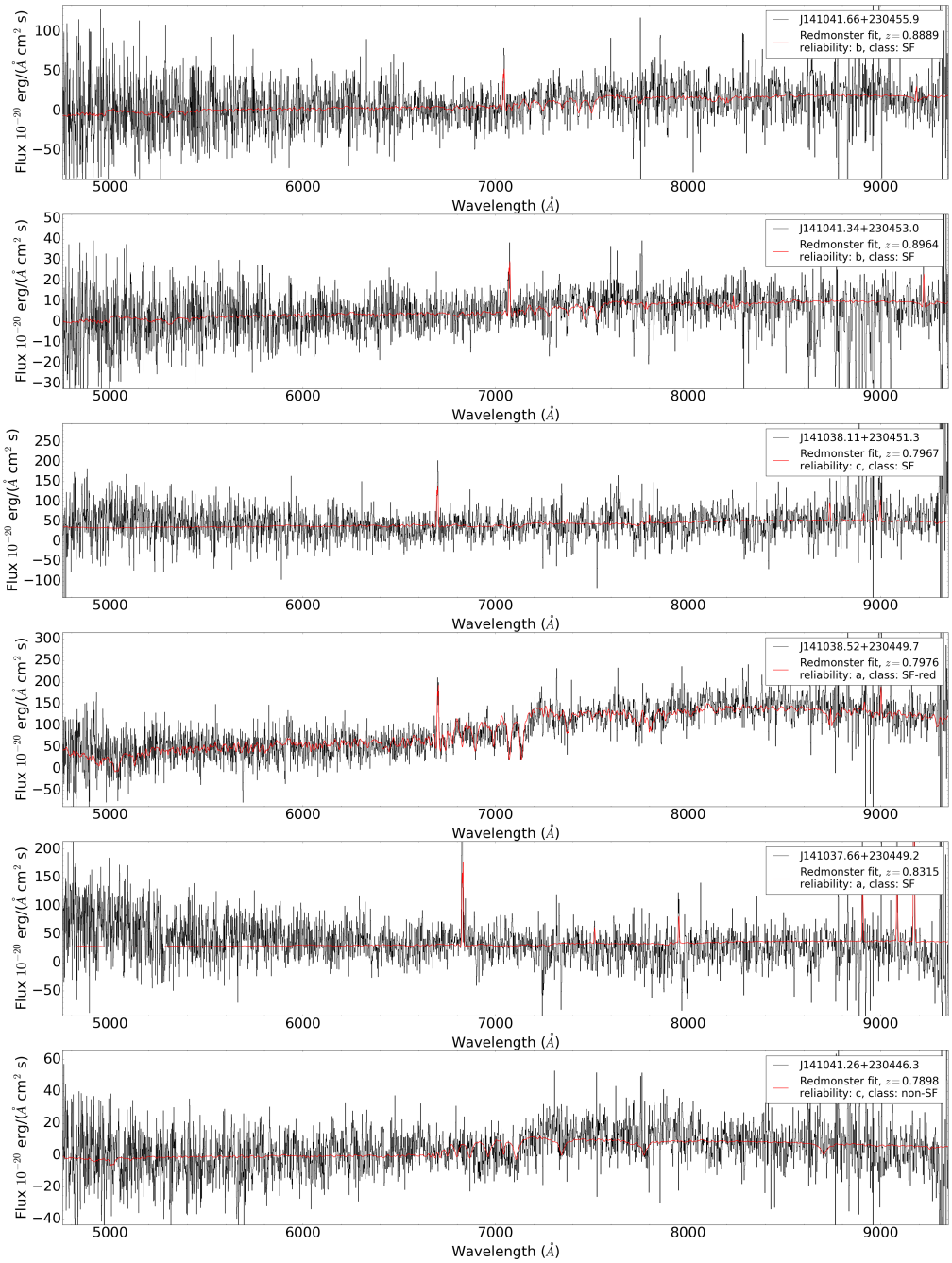

Figure D.5: Spectra characterized using Redmonster software

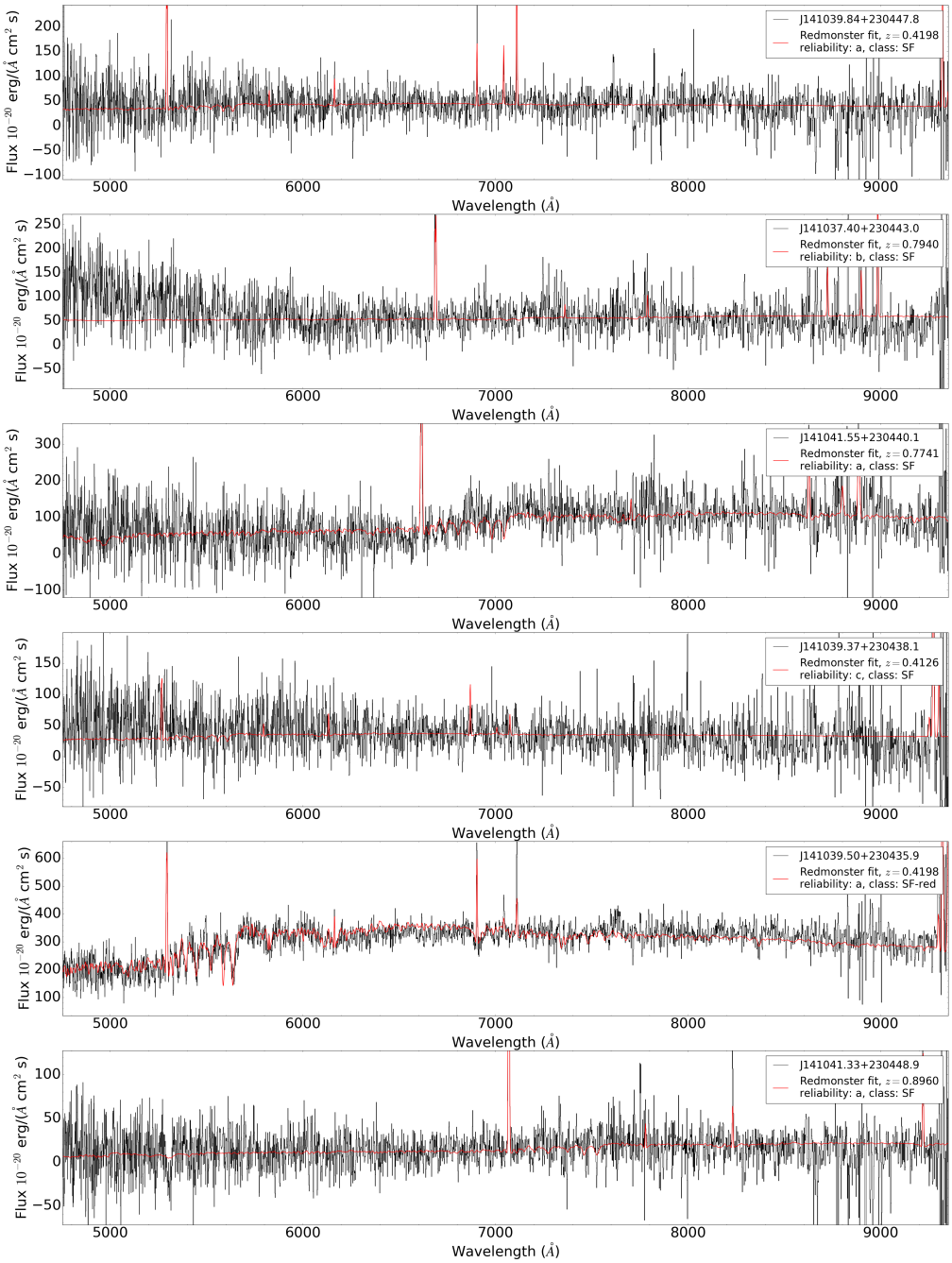

Figure D.6: Spectra characterized using Redmonster software

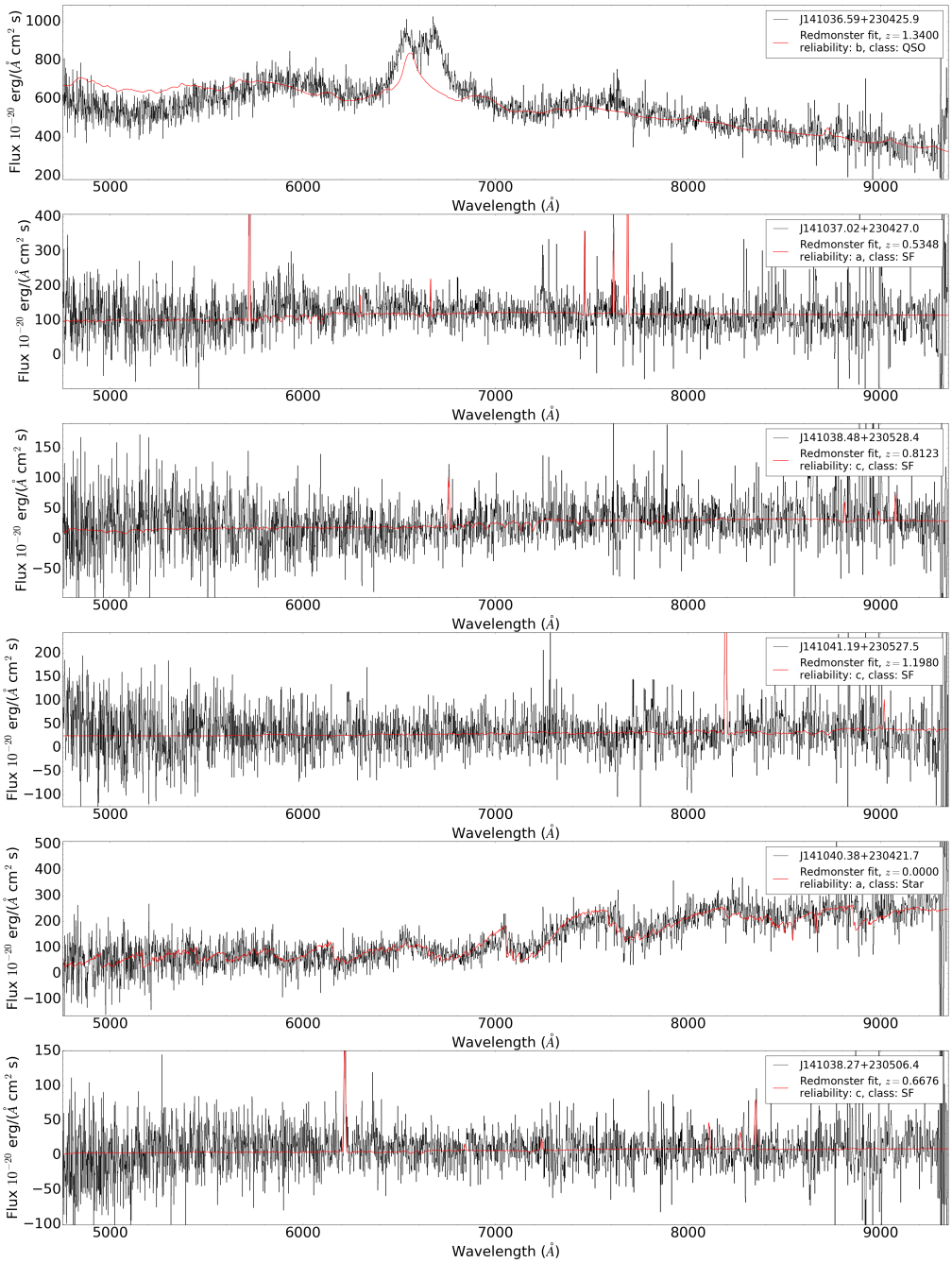

Figure D.7: Spectra characterized using Redmonster software

Appendix E

Re-analysis of BLAs reported by Tejos et al. 2016

In order to test for potential systematic errors in the characterization of BLAs by Tejos et al. (2016), here we have revisited their identifications and fit parameters. In particular, we repeated their analyses using the following:

- *Different data reduction* For our comparison we used the reduced Q1410 HST/COS data provided by the MAST HST archive[1] (referred to as 'new data') as opposed to the custom reduction done by Tejos et al. (2016, referred to as 'old data'). We note that the 'old data' has slightly higher signal-to-noise than the 'new data'.

- *Different continuum level estimation* For our comparison we used an independent estimation of the continuum level obtained from the 'new data' (referred to as 'new continuum') as opposed to the old continuum estimation described by Tejos et al. (2016, referred to as 'old continuum').

[1] `https://archive.stsci.edu/hst/`

- *Different Voigt profile fitting software* For our comparison we used VEEPER[2] as opposed to VPFIT[3] used by Tejos et al. (2016).

From the above, we performed the following combinations to define a set of new experiments: (a) new data and new continuum, (b) old data and new continuum, and (c) old data and old continuum, all of which performed using the new software VEEPER. Figure E.1 shows the obtained parameters for the putative BLAs from our different experiments and how these compare to those reported by Tejos et al. (2016). We see that, with the exception the absorption feature at $z = 0.3502$, all absorption features have systematic variations well below (or consistent) with the level of reported statistical uncertainties. The putative BLA at $z = 0.3502$ is the less constrained one as it may be superimposed to a complex narrow HI system and its absorption profile is degenerate with that of the narrow component. Indeed, in experiment (a) this absorption feature was fit with a very narrow line (Doppler parameter $b < 10\,\mathrm{kms}$) casting doubt on it being a genuine BLA. In any case, this feature has been also excluded from our 'clean BLA sample' (for the estimation of the filament baryon fraction in Section 5.2) on the basis of the existence of a potential galaxy counterpart (see Section 4.2).

[2]Mainly developed by J. Burchett; available at `https://github.com/jnburchett/veeper`.

[3]Developed by R.F.Carswell and J.K.Webb; available at `http://www.ast.cam.ac.uk/~rfc/vpfit.html`.

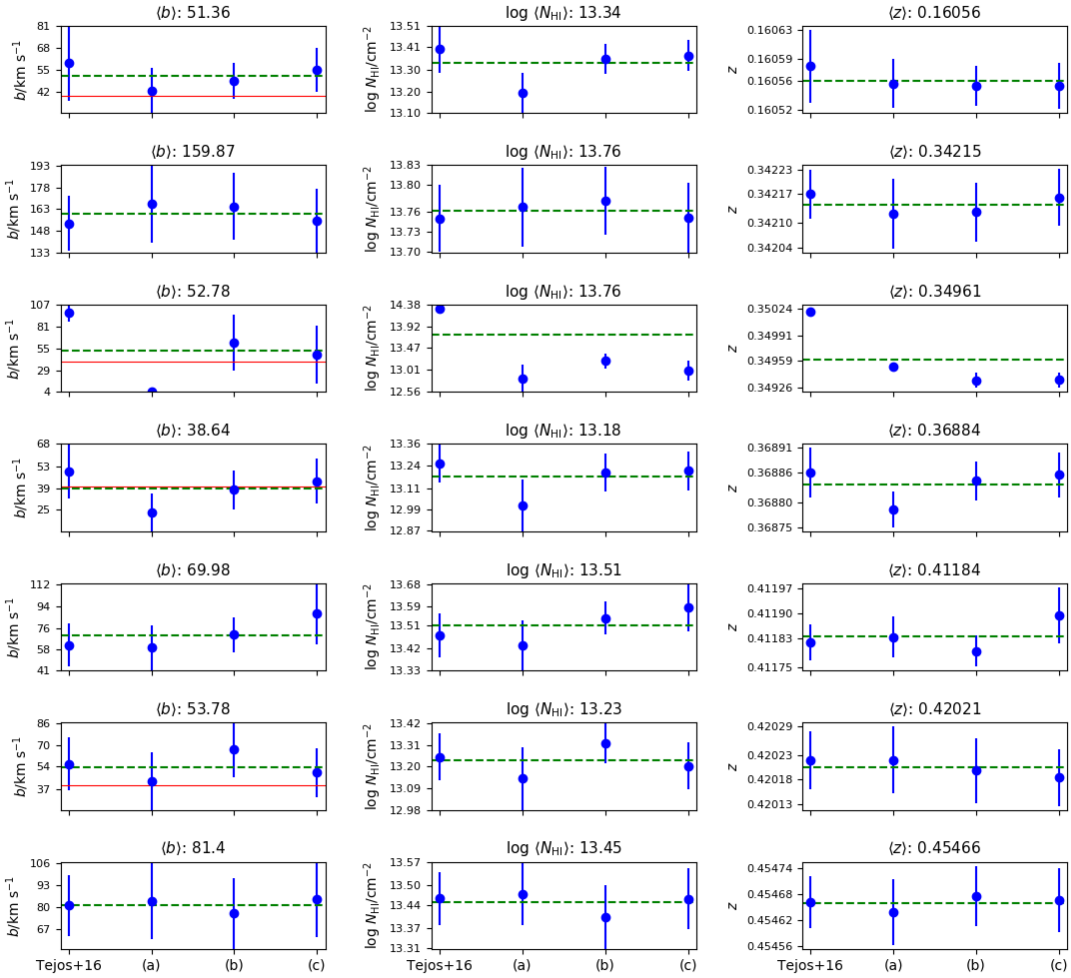

Figure E.1: Systematic comparison between the parameters obtained for the BLAs in our sample using a different data reduction, an independent continuum level estimation and a different Voigt profile fitting software. (a), (b) and (c) represent different combination of these variables respect to those used in Tejos et al. (2016). With the exception of the absorption feature at $z = 0.3502$, all absorption features have systematic variations consistent with the level of reported statistical uncertainties. More datails in Section 4.3)

Appendix F

PyMUSE: a Python package for VLT/MUSE data analysis

To perform the analysis presented in this thesis, we have developed PyMUSE (Pessa et al. 2018), a Python package for MUSE data analysis. It is well suited for deep field sources catalog and provides a set of routines focused for a systematic analysis to the data. It is intended to be used together with some other commonly used software for data analysis but it can still be useful to explore a data set by itself. PyMUSE was presented in the Astronomical Data Analysis Software and Systems (ADASS) XXVII by a focus demonstration and its current version can be found and downloaded from `https://github.com/ismaelpessa/PyMUSE`. Here we will describe some of the more important features of PyMUSE.

F.1 PyMUSE subroutines

F.1.1 Spectrum extraction

The main goal of PyMUSE is versatility at getting a spectrum. The aperture of extraction for a given source can be defined by a variety of manners:

- Elliptical set of parameters (x_c, y_c, a, b, θ).
- DS9 regions.
- Interactive canvas.

Fig. F.1 shows an example of how DS9 can be used to define apertures to extract a spectrum. Once the aperture is defined, the combination of the spaxels[1] inside the aperture can be done in a set of different ways:

- Sum, median and mean.
- Sum of the brightest X% of the spaxels inside the aperture.
- Weighted sum of the spaxels by a bright profile, either obtained from the MUSE white image or from a Gaussian profile.
- Weighted sum by the inverse of the variances (spatially or spectral).
- Combinations of the last 2 points.

F.1.2 Image creation

Users can use PyMUSE routines to create different kinds of images according to their needs.

- Filtered images to do photometry, by convolving the spectral axis of the datacube with SDSS or Johnson photometric filters is possible (customized filters can also be used). This feature can be very useful to characterize in detail sources in the field.
- "Emission line filter" at different redshifts can be useful to detect faint star-forming galaxies that could be not detectable in the white image and can help the user to perform a complete analysis.

[1]We refer to spaxels as the pixels defined in the spatial direction.

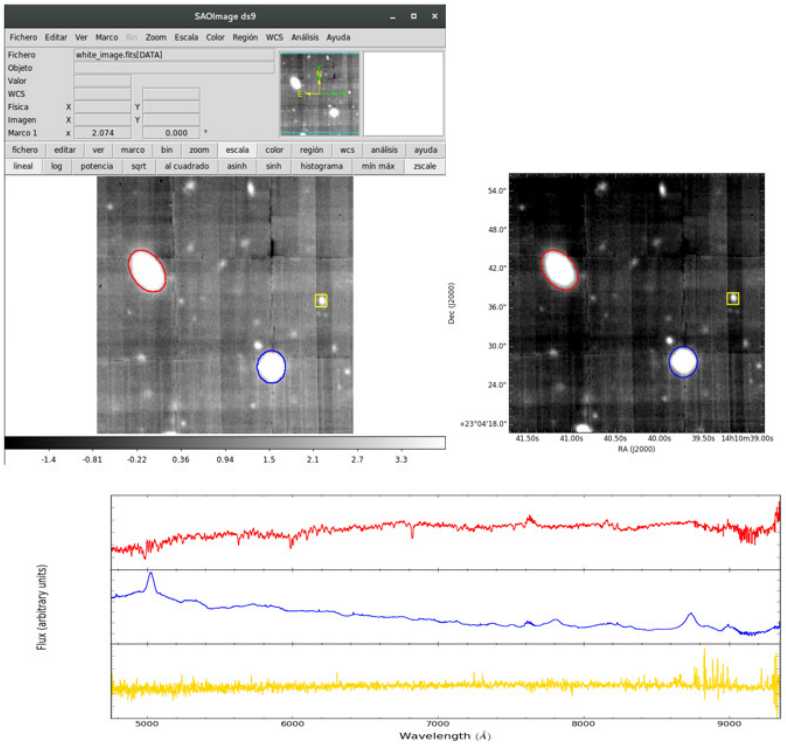

Figure F.1: Example of defining apertures using a DS9 region file. *Upper-Left*: Original regions defined in DS9. *Upper-rigth*: PyMUSE interface when the region file is given as input. *Lower*: Output spectra of the three regions extracted using the weighted sum mode based on the white profile.

- Smoothed and Masked images are also supported. The mask can be defined simply by a DS9 region file.

F.1.3 Compatibilities with external software

DS9

A useful PyMUSE utility for a systematic analysis is to receive as an input a DS9 region file containing the apertures of interest. The user can select a set of regions and immediately save the corresponding 1-D spectra for a posterior analysis.

SExtractor

The user can perform a systematic search of sources using SExtractor (Bertin & Arnouts 1996). In this case, the generated catalog can be used as a PyMUSE input to extract the 1-D spectra. The user can use this feature even if SExtractor is run in an image different than the MUSE image (astrometry should be checked in this case). Using SExtractor in a filtered image described in Section F.1.2 permit the user to simultaneously build a photometric and spectroscopic catalog of sources in the field.

MUSELET

MUSELET (for MUSE Line Emission Tracker) is an emission line galaxy detection tool based on SExtractor from MPDAF (Bacon et al. 2016) (MUSE Python Data Analysis Framework), `http//mpdaf.readthedocs.io/en/latest/muselet.html`). PyMUSE allow the user the extraction of a set spectra given a MUSELET output fits table. By doing this, the user can include on its survey very faint galaxies that may not be visible in the white image.

Redmonster

Redmonster software (Hutchinson et al. 2016) is a set of Python utilities for redshift measurement and classification of 1-D spectra by performing χ^2 minimization respect to a set of modulated theoretical models. The user can set the output spectra of PyMUSE to be directly used as Redmonster inputs. Figure F.2 shows the final redshifts and classification obtained by Redmonster for the spectra used in the example above.

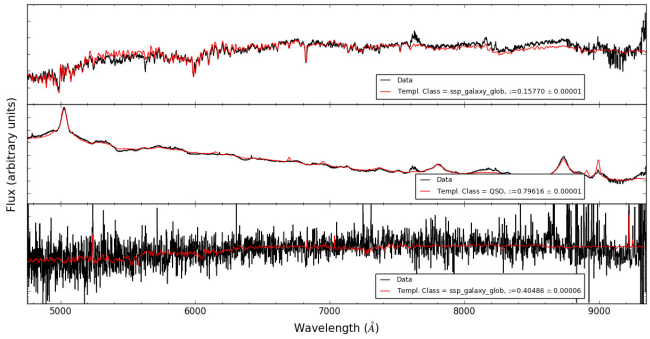

Figure F.2: Redmonster outputs for the 1-D spectra obtained from the apertures shown in Figure F.1.

Bibliography

Aragón-Calvo, M. A., van de Weygaert, R., & Jones, B. J. T. 2010, MNRAS, 408, 2163

Astropy Collaboration, Robitaille, T. P., Tollerud, E. J., et al. 2013, A&A, 558, A33

Bacon, R., Vernet, J., Borisova, E., et al. 2014, The Messenger, 157, 13

Bacon, R., Piqueras, L., Conseil, S., Richard, J., & Shepherd, M. 2016, Astrophysics Source Code Library, ascl:1611.003

Bertin, E., & Arnouts, S. 1996, A&AS, 117, 393

Bonamente, M., Nevalainen, J., Tilton, E., et al. 2016, MNRAS, 457, 4236

Borthakur, S., Heckman, T., Tumlinson, J., et al. 2016, ApJ, 833, 259

Bruzual, G., & Charlot, S. 2003, MNRAS, 344, 1000

Cautun, M., van de Weygaert, R., Jones, B. J. T., & Frenk, C. S. 2014, MNRAS, 441, 2923

Cen, R., & Ostriker, J. P. 1999, ApJ, 514, 1

Chabrier, G. 2003, PASP, 115, 763

Cid Fernandes, R., Mateus, A., Sodré, L., Stasińska, G., & Gomes, J. M. 2005, MNRAS, 358, 363

Colberg, J. M., Krughoff, K. S., & Connolly, A. J. 2005, MNRAS, 359, 272

Coleman, G. D., Wu, C.-C., & Weedman, D. W. 1980, ApJS, 43, 393

Danforth, C. W., Stocke, J. T., & Shull, J. M. 2010, ApJ, 710, 613

Davé, R., Cen, R., Ostriker, J. P., et al. 2001, ApJ, 552, 473

Fang, T., & Bryan, G. L. 2001, ApJ, 561, L31

Fang, T., Croft, R. A. C., Sanders, W. T., et al. 2005, ApJ, 623, 612

Fukugita, M., Hogan, C. J., & Peebles, P. J. E. 1998, ApJ, 503, 518

González, R. E., & Padilla, N. D. 2010, MNRAS, 407, 1449

de Graff, A, Cai, Y, Heymans, C, Peacock, John, 2017, arXiv:1709.10378

Hattori, S., Ota, N., Zhang, Y.-Y., Akamatsu, H., & Finoguenov, A. 2017, PASJ, 69, 39

Hutchinson, T. A., Bolton, A. S., Dawson, K. S., et al. 2016, AJ, 152, 205

Le Fèvre, O., Vettolani, G., Garilli, B., et al. 2005, A&A, 439, 845

Lehner, N., Savage, B. D., Richter, P., et al. 2007, ApJ, 658, 680

Li, H., Ge, J., Mao, S., et al. 2017, ApJ, 838, 77

McNaught-Roberts, T., Norberg, P., Baugh, C., et al. 2014, MNRAS, 445, 2125

Moster, B. P., Somerville, R. S., Maulbetsch, C., et al. 2010, ApJ, 710, 903

McQuinn, M. 2016, ARA&A, 54, 313

O'Meara, J. M., Lehner, N., Howk, J. C., et al. 2015, AJ, 150, 111

Penton, S. V., Stocke, J. T., & Shull, J. M. 2004, ApJS, 152, 29

Persic, M., & Salucci, P. 1992, MNRAS, 258, 14P

Pessa, I., Tejos, N., & Moya, C. 2018, arXiv:1803.05005

Planck Collaboration, Ade, P. A. R., Aghanim, N., et al. 2016, A&A, 594, A13

Prochaska, J. X., & Tumlinson, J. 2009, Astrophysics and Space Science Proceedings, 10, 419

Prochaska, J. X., Weiner, B., Chen, H.-W., Mulchaey, J., & Cooksey, K. 2011, ApJ, 740, 91

Prochaska, J. X., Tejos, N., Crighton, N., Burchett, J., & Tuo-Ji. 2016, linetools/linetools: Second major release, doi:10.5281/zenodo.168270

Rauch, M., Haehnelt, M. G., & Steinmetz, M. 1997, ApJ, 481, 601

Reed, D. S., Bower, R., Frenk, C. S., Jenkins, A., & Theuns, T. 2007, MNRAS, 374, 2

Richter, P., Savage, B. D., Tripp, T. M., & Sembach, K. R. 2004, ApJS, 153, 165

Richter, P., Fang, T., & Bryan, G. L. 2006, A&A, 451, 767

Richter, P., Savage, B. D., Sembach, K. R., & Tripp, T. M. 2006, A&A, 445, 827

Savage, B. D., Kim, T.-S., Wakker, B. P., et al. 2014, ApJS, 212, 8

Sawala, T., Frenk, C. S., Fattahi, A., et al. 2016, MNRAS, 456, 85

SDSS Collaboration, Albareti, F. D., Allende Prieto, C., et al. 2016, arXiv:1608.02013

Shen, L., Miller, N. A., Lemaux, B. C., et al. 2017, MNRAS, 472, 998

Shull, J. M., Smith, B. D., & Danforth, C. W. 2012, ApJ, 759, 23

Soto, K. T., Lilly, S. J., Bacon, R., Richard, J., & Conseil, S. 2016, MNRAS, 458, 3210

Stocke, J. T., Keeney, B. A., Danforth, C. W., et al. 2014, ApJ, 791, 128

Sutherland, R. S., & Dopita, M. A. 1993, ApJS, 88, 253

Tanimura, H, Hinshaw, G, Van Waerbeke, L, Ma, Y, Maed, A, Hojjati, A, TrÃűster, T. 2017, arXiv:1709.05024

Taylor, E. N., Hopkins, A. M., Baldry, I. K., et al. 2011, MNRAS, 418, 1587

Tejos, N., Prochaska, J. X., Crighton, N. H. M., et al. 2016, MNRAS, 455, 2662

Tepper-García, T., Richter, P., Schaye, J., et al. 2012, MNRAS, 425, 1640

Tilton, E. M., Danforth, C. W., Shull, J. M., & Ross, T. L. 2012, ApJ, 759, 112

Tripp, T. M., Bowen, D. V., Sembach, K. R., et al. 2006, Astrophysics in the Far Ultraviolet: Five Years of Discovery with FUSE, 348, 341

Wakker, B. P., Hernandez, A. K., French, D. M., et al. 2015, ApJ, 814, 40

Weinberg, D. H., Miralda-Escudé, J., Hernquist, L., & Katz, N. 1997, ApJ, 490, 564

Williams, R. J., Mulchaey, J. S., & Kollmeier, J. A. 2013, ApJ, 762, L10

Zucca, E., Ilbert, O., Bardelli, S., et al. 2006, A&A, 455, 879